

UNSW
AUSTRALIA

SCHOOL OF ELECTRICAL ENGINEERING
AND TELECOMMUNICATIONS

Joint Non-Uniform Sparse MIMO Array and Resource Allocation Design for Integrated Sensing and Communication

by

Chongyi Li

Thesis submitted as a requirement for the degree

Master of Engineering (Electrical Engineering)

Submitted: August 2026
Supervisors: Derrick Wing Kwan Ng and Shaokang Hu

Abstract

Integrated sensing and communication (ISAC) is expected to support future wireless systems by allowing communication and sensing functions to share spectrum, hardware, and transmitted signals. Large antenna apertures improve both spatial multiplexing and angular estimation, but densely populated arrays incur substantial radio-frequency hardware, energy, and computational costs. This thesis investigates the joint design of a dynamic non-uniform sparse antenna array and downlink beamforming for a multi-user multiple-input multiple-output ISAC system. A binary activation vector selects a limited number of elements from a larger candidate grid, while user-specific beamformers determine the shared transmit covariance. Communication performance is measured by the achievable sum rate subject to per-user signal-to-interference-plus-noise ratio requirements, whereas sensing performance is represented by a weighted Cramér–Rao bound derived from the Fisher information matrix. The resulting mixed-integer non-convex problem balances the two functions under transmit-power and hardware constraints. A low-complexity alternating-optimisation framework is developed: successive convex approximation is used for the beamforming update, and semidefinite relaxation followed by feasible rounding is used for sparse-array selection. Convergence and computational requirements are analysed. The formulation provides a reproducible basis for evaluating adaptive sparse arrays against dense and fixed-array benchmarks; the numerical evaluation is reserved for the subsequent simulation study.

Acknowledgements

I would like to thank my supervisors, Professor Derrick Wing Kwan Ng and Dr Shaokang Hu, for their guidance, technical advice, and continued support throughout this project. I also thank my family and friends for their encouragement during my studies.

Abbreviations

6G Sixth-generation wireless networks

AO Alternating optimisation

AWGN Additive white Gaussian noise

BS Base station

CRB Cramér–Rao bound

CSI Channel state information

DFRC Dual-functional radar-communication

FIM Fisher information matrix

ISAC Integrated sensing and communication

LMI Linear matrix inequality

MIMO Multiple-input multiple-output

MRC Maximum-ratio combining

NUSA Non-uniform sparse array

QoS Quality of service

RF Radio frequency

SCA Successive convex approximation

SDP Semidefinite program

SDR Semidefinite relaxation

SINR Signal-to-interference-plus-noise ratio

ULA Uniform linear array

UPA Uniform planar array

Contents

Acknowledgements i

Abbreviations ii

Contents iv

1 Introduction 1

1.1 Background 1

1.2 Aim and Objectives 3

1.3 Thesis Outline 4

1.4 Notation 4

2 Literature Review 5

2.1 Sparse MIMO for Spatial Multiplexing and Interference Suppression 5

2.2 Sparse Channel Estimation for Spatially Non-Stationary Massive MIMO 6

2.3 Waveform Optimisation for Compressed-Sensing-Based 2D MIMO Radar . . . 8

2.4 Hardware-Friendly Sparse MIMO Array Optimisation 9

2.5 Compressed-Sampling mmWave Massive-MIMO ISAC 9

2.6 Sparse Arrays and Sparse Pilots for UAV Sensing 11

2.7 Reconfigurable Antennas and Joint ISAC Design 11

2.8 Joint Beamforming, Sensing Accuracy, and Resource Allocation 12

2.9 Implications for Non-Uniform Sparse ISAC Arrays 13

2.10 Summary and Research Gap 14

3 System Model and Performance Metrics 16

3.1 System Architecture 16

3.2 Array Response 17

3.3 Communication Channel Model . . . 18
3.4 Transmit and Received Signal Models . . . 19
3.5 Communication SINR and Achievable Rate . . . 19
3.6 Sensing SINR . . . 20
3.7 Fisher Information and Cramér–Rao Bound . . . 20
3.8 Modelling Assumptions . . . 21

4 Joint Optimisation Problem Formulation 22
4.1 Joint Design Formulation . . . 22
4.2 Objective-Function Expansion and Convexity . . . 23
4.3 Convexity Analysis and Constraint Reformulation . . . 24
4.4 Reformulation Strategy . . . 25

5 Low-Complexity Suboptimal Solution 27
5.1 Alternating-Optimisation Framework . . . 27
5.2 Subproblem 1: Transmit Beamforming Design . . . 27
5.2.1 Fixed-array quantities and matrix lifting . . . 27
5.2.2 Transformation of C1 . . . 28
5.2.3 Transformation of C2–C4 . . . 28
5.2.4 SCA transformation of the communication objective . . . 29
5.2.5 Transformation of the sensing objective . . . 29
5.2.6 Resulting beamforming subproblem . . . 30
5.3 Subproblem 2: Non-Uniform Antenna Selection . . . 30
5.3.1 Quadratic activation form and lifting . . . 30
5.3.2 Transformation of C1 . . . 31
5.3.3 Transformation of C2–C4 . . . 31
5.3.4 SCA transformation of the communication objective . . . 32
5.3.5 Transformation of the sensing objective . . . 32
5.3.6 Resulting antenna-selection subproblem . . . 32
5.4 Binary Recovery and Feasibility Restoration . . . 33
5.5 Overall Suboptimal Algorithm . . . 34
5.6 Convergence Analysis . . . 35
5.7 Computational Complexity Analysis . . . 35

5.8 Implementation and Reproducibility Requirements 36

6 Simulation Results and Discussion **37**

7 Conclusion and Future Work **45**

Bibliography **47**

Chapter 1

Introduction

1.1 Background

Integrated sensing and communication (ISAC) enables a wireless system to use a common spectrum, waveform, and infrastructure for data transmission and environmental sensing. Information is delivered through the communication links, while target parameters are extracted from the scattered echoes of the same transmitted signal. This integration can substantially improve spectral, energy, and hardware efficiency, and allows the sensing and communication functions to assist one another [1, 2].

The rapid growth of connected devices and emerging applications, including high-precision localisation, autonomous driving, industrial Internet of Things, and digital twins, places stringent requirements on sixth-generation (6G) wireless networks. In addition to ultra-high data rates, ultra-reliable transmission, and massive connectivity, future systems are expected to provide centimetre- or even millimetre-level sensing and positioning accuracy [3]. ISAC has consequently been recognised as a key enabling technology for 6G because it unifies communication and sensing within a shared radio architecture [4].

Multiple-input multiple-output (MIMO) technology is central to this vision. By employing multiple transmit and receive antennas, MIMO systems improve spectral efficiency, channel capacity, spatial multiplexing, and angular discrimination [5]. In a conventional dense array, adjacent antenna elements are normally separated by one half-wavelength and arranged as a uniform linear array or uniform planar array. Such critically spaced structures avoid spatial aliasing and provide effective beam control [6]. Nevertheless, increasing the array size also increases the required number of radio-frequency chains, phase shifters, data converters, and optimisation

variables. At millimetre-wave and prospective sub-terahertz frequencies, the resulting hardware cost, power consumption, and signal-processing burden can become prohibitive.

Sparse MIMO arrays provide a practical alternative. By distributing a smaller number of active elements over a larger physical aperture, a sparse array can produce a narrower main lobe, improve angular resolution, and create additional spatial degrees of freedom without requiring the hardware of a fully populated dense array [7, 8]. Sparse arrays may be uniformly spaced, with an inter-element distance greater than one half-wavelength, or non-uniformly spaced, as in minimum-redundancy, nested, and coprime arrays. Their benefits are accompanied by grating lobes, angular ambiguity, mutual-coupling effects, and a more difficult array-design problem [9].

Recent studies have begun to combine sparse arrays with ISAC. The compressed-sampling mmWave massive-MIMO architecture in [10] demonstrates that a large sparse aperture can improve angular resolution while reducing acquisition overhead. The analysis in [8] further shows that sparse spacing can enhance spatial multiplexing, particularly in near-field channels. A wide sparse radar receiver and an orthogonal matching-pursuit algorithm with support refinement are developed in [7] to mitigate angular ambiguity. These contributions establish the value of sparse apertures, but their array geometries are prescribed and the communication and sensing resources are not jointly adapted to the instantaneous users and targets.

Related work on waveform and array optimisation reaches a similar limitation. The two-dimensional compressed-sensing radar in [11] optimises the sensing waveform to improve sparse angular recovery, while the grid-based sparse-array framework in [12] balances beamwidth, sidelobe level, field of view, and hardware constraints. Both studies are radar-centred and do not include the multi-user communication requirements that define an ISAC system. Consequently, the joint and dynamic design of a non-uniform sparse array and the shared transmit signal remains an open problem.

This thesis addresses that problem by treating the active array geometry as an optimisable radio resource. A binary activation vector selects a non-uniform subset of a larger candidate grid, and this selection is jointly designed with the downlink beamformers. Communication performance is measured by the multi-user sum rate under per-user signal-to-interference-plus-noise ratio (SINR) requirements, whereas sensing performance is represented by a weighted Cramér–Rao bound (CRB). Since the binary activation variables multiply the beamformers, the SINR expressions contain coupled quadratic ratios, and the Fisher information matrix depends on the active transmit covariance, the resulting design is a mixed-integer non-convex optimisation

problem.

1.2 Aim and Objectives

The principal aim of this thesis is to develop a unified and computationally tractable framework for the joint design of a dynamic non-uniform sparse antenna array and the shared transmit beamforming in a multi-user MIMO-ISAC system. The proposed design seeks to improve the communication–sensing trade-off while satisfying user quality-of-service, transmit-power, and active-radio-frequency-chain requirements.

To achieve this aim, the following objectives are pursued:

1. establish a system model that integrates dynamic antenna activation with the communication channel, common ISAC signal, target-echo model, SINR, achievable rate, Fisher information, and CRB;

2. formulate a weighted communication–sensing optimisation problem that jointly determines the antenna activation pattern and user beamformers;

3. identify explicitly the sources of non-convexity in the objective function and every constraint;

4. develop an alternating-optimisation algorithm in which the beamforming and antenna-selection variables are handled through suitable lifting, successive convex approximation, and semidefinite relaxation techniques;

5. establish the convergence behaviour and computational complexity of the complete algorithm; and

6. evaluate the dynamic non-uniform sparse array against dense, fixed sparse, random sparse, communication-only, and sensing-only benchmark schemes.

The principal value added by this work is the joint treatment of physical aperture selection and signal design. In contrast to a fixed sparse geometry selected before beamforming, the proposed framework allows the active aperture to adapt to the current user channels, target directions, sensing requirements, and communication–sensing preference.

1.3 Thesis Outline

Chapter 2 reviews sparse MIMO spatial multiplexing, sparse channel estimation, waveform and array optimisation, compressed-sampling ISAC, and sparse-array sensing, before identifying the research gap addressed by this thesis. Chapter 3 presents the candidate-array geometry, communication and sensing signal models, and the performance metrics used in the subsequent optimisation. Chapter 4 formulates the joint mixed-integer problem and analyses the non-convexity of its objective and constraints. Chapter 5 develops the alternating-optimisation solution, including the beamforming and antenna-selection subproblems, binary recovery, convergence, computational complexity, and the complete algorithm. Chapter 6 is reserved for the numerical results and their discussion. Finally, Chapter 7 will summarise the conclusions and value added after the numerical study has been completed.

1.4 Notation

Italic lower-case letters denote scalars, bold lower-case letters denote column vectors, and bold upper-case letters denote matrices. Calligraphic upper-case letters denote sets. The sets of real and complex $m \times n$ matrices are denoted by $\mathbb{R}^{m\times n}$ and $\mathbb{C}^{m\times n}$, respectively. The transpose, complex conjugate, and Hermitian transpose of a matrix are represented by $(\cdot)^{\mathsf{T}}$, $(\cdot)^{*}$, and $(\cdot)^{\mathsf{H}}$, respectively. The operators $|\cdot|$ and $\|\cdot\|_2$ denote the absolute value and Euclidean norm, while $\mathbb{E}\{\cdot\}$ and $\Re\{\cdot\}$ denote statistical expectation and the real part of a complex quantity. The trace, rank, and diagonal operators are written as $\mathrm{tr}(\cdot)$, $\mathrm{rank}(\cdot)$, and $\mathrm{diag}(\cdot)$, respectively. The symbol $\otimes$ denotes the Kronecker product, $\boldsymbol{I}_N$ denotes the $N \times N$ identity matrix, and $\mathbf{0}$ denotes an all-zero vector or matrix of appropriate dimension. For a Hermitian matrix $\boldsymbol{X}$, $\boldsymbol{X} \succeq \mathbf{0}$ indicates that $\boldsymbol{X}$ is positive semidefinite. Finally, $\mathcal{CN}(\boldsymbol{\mu}, \boldsymbol{R})$ denotes a circularly symmetric complex Gaussian distribution with mean $\boldsymbol{\mu}$ and covariance $\boldsymbol{R}$.

Chapter 2

Literature Review

2.1 Sparse MIMO for Spatial Multiplexing and Interference Suppression

The work in [8] provides a theoretical examination of how sparse antenna spacing changes the spatial-multiplexing properties of MIMO systems in both far-field and near-field regimes. Classical array design normally restricts the inter-element spacing to $\lambda_c/2$ to avoid spatial aliasing. This rule follows from the far-field plane-wave model, however, and does not fully describe extremely large arrays operating in the radiative near field, where the phase curvature depends on both angle and distance.

For a transmit array with spacing $d > \lambda_c/2$, the distance from antenna m to user k is

$$r_{k,m} = \sqrt{r_k^2 + (md)^2 - 2r_k md \sin\theta_k}, \tag{2.1}$$

and the corresponding spherical-wave channel coefficient is

$$h_{k,m} = \frac{1}{r_{k,m}} \exp\left(-j\frac{2\pi}{\lambda_c} r_{k,m}\right). \tag{2.2}$$

Unlike a plane-wave channel, this expression contains a distance-dependent phase curvature across the array. For a K-user downlink, the received signal is represented as

$$\boldsymbol{y} = \boldsymbol{H}\boldsymbol{x} + \boldsymbol{n}, \qquad \boldsymbol{H} \in \mathbb{C}^{K\times M}, \tag{2.3}$$

where the entries of $\boldsymbol{H}$ follow the spherical-wave model above.

The eigenvalue distribution of $\boldsymbol{H}\boldsymbol{H}^{\mathrm{H}}$ is used in [8] to quantify the effective spatial degrees of freedom. The analysis shows that increasing the array spacing can increase the effective channel

rank in the near field, thereby providing additional multiplexing gain even for line-of-sight propagation. Although sparse spacing produces grating lobes, randomly located users rarely coincide exactly with all grating-lobe directions. Consequently, sparse MIMO can improve user separability rather than serving only as a hardware-reduction mechanism.

This study is restricted to communication performance. It does not incorporate a sensing model, sensing-accuracy constraint, or joint communication–sensing objective. Moreover, the investigated arrays are uniformly sparse and their spacing is prescribed rather than optimised. The work therefore establishes the communication benefit of a large sparse aperture but does not determine how a non-uniform activation pattern should be selected for ISAC.

The near-field perspective is further supported by an analytical framework for the effective degrees of freedom of extremely large-scale MIMO (XL-MIMO) arrays [13]. Such analyses clarify why aperture, range, and array sampling should be treated separately: enlarging the physical aperture can provide additional spatial discrimination, but the actual gains depend on channel geometry and the locations of the radiators. Robust spherical-wavefront beamforming for near-field ISAC has subsequently been considered from a distance–angle perspective [14], while hybrid near-/far-field six-dimensional movable-antenna design has exploited directional sparsity to adapt the physical antenna configuration [15]. The former emphasises field-consistent beamforming and the latter adds physical positioning and orientation flexibility. Neither establishes that an arbitrary sparse activation pattern is optimal for the particular joint sum-rate–CRB objective considered here; rather, they underscore the need to preserve the correct array manifold when jointly optimising antenna selection and beams.

2.2 Sparse Channel Estimation for Spatially Non-Stationary Massive MIMO

Sparse channel estimation for frequency-division-duplex massive MIMO under spatial non-stationarity is considered in [16]. Conventional compressed-sensing estimators commonly assume that all antennas observe the same propagation clusters and hence share a common delay-domain support. For a physically large array, different regions may instead observe different cluster subsets. This spatial non-stationarity changes the received power, delay spread, angular spread, and cluster visibility across the aperture.

For a base station with M antennas, the channel impulse response from antenna m is written

as

$$\boldsymbol{h}_m = [h_m(1), h_m(2), \ldots, h_m(L)]^{\mathsf{T}}. \tag{2.4}$$

With pilot vector $\boldsymbol{x}_m$ and partial DFT matrix $\boldsymbol{F}$, the received pilot observation is

$$\boldsymbol{y} = \sum_{m=1}^{M} \operatorname{diag}(\boldsymbol{x}_m)\boldsymbol{F}\boldsymbol{h}_m + \boldsymbol{n}. \tag{2.5}$$

Stacking all antenna channels gives

$$\boldsymbol{y} = \boldsymbol{A}\boldsymbol{h} + \boldsymbol{n}, \tag{2.6}$$

which can be rearranged into the block-sparse form

$$\boldsymbol{y} = \boldsymbol{\Phi}\boldsymbol{b} + \boldsymbol{n}. \tag{2.7}$$

A two-stage block-matching-pursuit method is then applied. Candidate delay-support blocks are detected in the first stage, and a threshold-based refinement corrects the support errors caused by spatial non-stationarity. The proposed method achieves lower estimation error than common-support estimators when different parts of the array observe different clusters.

Although this work demonstrates the importance of modelling a large physical aperture correctly, it remains a communication-side channel-estimation study. The array is critically spaced, antenna activation is not optimised, and no sensing function or hardware-performance trade-off is considered. Its relevance to the present thesis lies in showing that a dynamically selected large aperture may alter channel statistics and that perfect common-support assumptions should not be adopted without qualification.

More recent contributions refine this channel-acquisition viewpoint. Sensing-assisted sparse channel recovery for massive antenna systems [17] and sensing-enhanced channel estimation for near-field XL-MIMO [18] explicitly exploit the information shared between propagation inference and sensing. Model-based deep learning for spatially non-stationary XL-MIMO estimation [19] and near-field spatial-domain channel extrapolation [20] address the challenge of obtaining channel information across large apertures without treating every antenna observation as independent. In another hardware architecture, partially decoupled atomic-norm estimation is proposed for RIS-aided MIMO channels [21]. Although their channel models and estimators are not interchangeable, these studies collectively indicate that channel recovery, array geometry, and the visibility of propagation paths should be considered together. The present thesis concentrates instead on transmit-array activation and resource allocation, and therefore regards channel acquisition and its associated overhead as important qualifications when interpreting performance obtained under assumed channel knowledge.

2.3 Waveform Optimisation for Compressed-Sensing-Based 2D MIMO Radar

The study in [11] investigates waveform optimisation for a compressed-sensing-based two-dimensional MIMO radar using an L-shaped array. Compressed sampling can reduce the sampling rate and data volume, but recovery accuracy depends strongly on the coherence of the sensing matrix, which is determined jointly by the waveform, array response, and sampling pattern.

Under a discretised azimuth–elevation grid, the target scene is represented by a sparse reflectivity vector $\boldsymbol{s} \in \mathbb{C}^G$, and the compressed observation is

$$\boldsymbol{y} = \boldsymbol{\Theta}\boldsymbol{s} + \boldsymbol{w}, \tag{2.8}$$

where $\boldsymbol{\Theta}$ is the effective sensing matrix. The waveform is designed to reduce the mutual coherence of $\boldsymbol{\Theta}$ subject to bandwidth and power constraints. Sparse Bayesian learning is used to recover the target coefficients through an iterative expectation–maximisation procedure. The optimised waveform provides lower angle-estimation error than non-optimised waveforms, particularly at high compression ratios and low SNR.

The work demonstrates that waveform and sparse-recovery design cannot be considered independently. Nevertheless, it is radar-centric: no communication signal or multi-user interference is included, and the L-shaped array remains dense and fixed. It therefore does not address the joint selection of array geometry and communication beamforming required in the present ISAC design.

The distinction between sensing-waveform design and communication-aware optimisation is also apparent in frequency-diverse-array (FDA) MIMO radar–communication coexistence, for which transceiver optimisation has been investigated [22]. Radar–communication coexistence is not identical to a fully shared ISAC transmitter: separately operating functions introduce interference-management questions, whereas a shared ISAC array must reconcile sensing information with the communication signal and its user-specific beams. This distinction motivates the common transmit-signal model adopted later in the thesis.

2.4 Hardware-Friendly Sparse MIMO Array Optimisation

Practical grid-based sparse MIMO arrays are studied in [12]. Classical nested and coprime arrays enlarge the difference co-array, but their analytical structures do not necessarily satisfy fabrication, minimum-spacing, mutual-coupling, or field-of-view constraints. The cited work consequently formulates a multi-objective design over a planar grid of candidate locations.

For a selected antenna subset $\mathcal{S}$, the far-field echo is modelled as

$$\boldsymbol{y}(\theta) = \alpha \boldsymbol{C}\boldsymbol{d}_{\mathcal{S}}(\theta) + \boldsymbol{w}, \tag{2.9}$$

where $\boldsymbol{C}$ represents mutual coupling. Beamwidth, peak sidelobe ratio, grating-lobe-limited field of view, and aperture effectiveness are mapped to individual desirability functions $D_k(\mathcal{S})$. The combined objective is

$$\underset{\mathcal{S}}{\text{maximize}} \quad D(\mathcal{S}) = \prod_{k=1}^{K} D_k(\mathcal{S})^{\omega_k}. \tag{2.10}$$

A genetic algorithm, gradient refinement, and learned initialisation are used to find implementable layouts. The resulting arrays provide favourable radar beampatterns while explicitly accounting for mutual coupling.

The framework illustrates the value of multi-objective sparse-array optimisation, but its objectives are exclusively sensing based. Communication spectral efficiency, user QoS, transmit beamforming, and dynamic switching are absent. The present work extends the underlying grid-selection concept to a shared communication–sensing signal and a CRB-based sensing metric.

The engineering relevance of hardware cost is also evident in antenna-selection research outside ISAC. For example, an uplink OFDMA antenna-selection strategy jointly addresses energy-efficiency considerations and competing system objectives [23]. Its selection variables optimise communication-side operation rather than radar resolution. The important transferable lesson is methodological: switching off antenna elements changes both the useful channel and the power consumption, so a sparse-array formulation should not maximise aperture or spectral efficiency without specifying the active-chain budget.

2.5 Compressed-Sampling mmWave Massive-MIMO ISAC

A comprehensive mmWave massive-MIMO ISAC architecture is developed in [10]. The dual-functional station contains a communication unit with a critically spaced UPA and a radar unit

with a widely spaced array. For an $N_x \times N_y$ planar array, the response is expressed as

$$\boldsymbol{d}_N(\theta^{\text{azi}}, \theta^{\text{ele}}) = \boldsymbol{d}(\mu_\theta; N_x) \otimes \boldsymbol{d}(\nu_\theta; N_y), \tag{2.11}$$

where $\mu_\theta = \cos\theta^{\text{azi}} \sin\theta^{\text{ele}}$ and $\nu_\theta = \sin\theta^{\text{azi}} \sin\theta^{\text{ele}}$. Increasing the element spacing enlarges the radar aperture but introduces angular ambiguity.

The work exploits sparsity in the angular, delay, and Doppler domains to reduce channel-estimation and sensing overhead. A compressed-sampling frame structure, hybrid beamforming strategy, and support-refinement algorithm are developed to resolve ambiguity by exploiting consistency between communication and radar observations. Simulations demonstrate that accurate sensing and communication can be obtained with reduced pilot overhead.

This study directly supports the feasibility of mmWave ISAC and motivates the sparse geometric channel adopted in Chapter 3. However, the transmit and receive geometries are fixed, and the study does not jointly optimise element activation, communication rate, sensing CRB, and hardware cost.

A complementary research direction exploits communication waveforms and temporal structure for sensing. Integrated radar-assisted orthogonal time-frequency space (OTFS) transmission for vehicular systems [24] and spatially spread OTFS-based ISAC [25] treat delay–Doppler structure as a means of supporting two functions with related signalling resources. Low-complexity ISAC precoding in the delay–Doppler domain [26] and dual-timescale sensing/channel estimation [27] extend this line by emphasising transmit processing and the distinct update rates of sensing and communication information. These contributions enrich the waveform-design dimension but do not, by themselves, choose a non-uniform subset of candidate planar antenna locations.

Sensing can also support beam tracking when channels change quickly. Bayesian joint radar–communication predictive beamforming [28] and learning-based predictive beamforming for vehicular ISAC [29] use sensing-derived information to anticipate channel and beam variations. These works are useful precedents for adapting radio resources to the scene; however, prediction over time differs from selecting an instantaneous spatial activation pattern under an RF-chain cap. In the present study, the geometry-selection problem is examined separately from time-varying channel prediction, so the numerical results should not be interpreted as accounting for beam-training or reconfiguration delays.

2.6 Sparse Arrays and Sparse Pilots for UAV Sensing

Sparse planar arrays and sparse pilot placement for UAV sensing are investigated in [30]. The antenna positions $\{\boldsymbol{s}_i\}$ generate the difference co-array

$$\mathcal{D}_{\mathcal{S}} = \{\boldsymbol{s}_i - \boldsymbol{s}_j \mid 1 \leq i, j \leq N\}, \tag{2.12}$$

whose size and continuity determine the number of resolvable targets. Sparse time–frequency pilots are additionally used for delay and Doppler estimation.

The reported results show that a sparse planar array can approach the direction-estimation performance of a dense UPA for a single target while using fewer physical elements. In multi-target cases, missing difference-co-array lags reduce the available degrees of freedom and degrade performance. This result is important for dynamic sparse ISAC: retaining aperture alone is insufficient, because the exact selected geometry determines ambiguity and multi-target resolution.

The work considers sensing without a simultaneous multi-user communication task, and the nested or coprime layouts are fixed. No joint optimisation of array geometry, pilot pattern, beamforming, and communication–sensing trade-off is provided.

Sensing performance also depends on which parameters must be resolved. Deep-learning-based near-field user localisation under wideband beam squint [31] and dual-polarised channel representations for localisation [32] highlight spatial or polarisation information beyond a conventional narrowband angle-only model. Coordinated beamforming for networked communication and multi-target localisation [33] further shows that sensing and positioning metrics may enter a network-level beamforming problem. These models differ in their observables and nuisance parameters. Accordingly, the CRB used in this thesis must be understood as a bound for the specified target parameters and signal model, not as a universal surrogate for every localisation or multi-target sensing task.

2.7 Reconfigurable Antennas and Joint ISAC Design

Recent research has treated antenna configurations, rather than only signal weights, as optimisation resources. The joint beamforming and port-selection design in [34] considers the spatial flexibility offered by fluid antenna ports, whereas pinching-antenna-assisted ISAC uses waveguide mode selection to alter the available radiation modes [35]. A broader survey of

fluid antenna technology [36] places such position-reconfigurable architectures in the context of emerging wireless systems. Although these approaches share the idea of spatial adaptation, fluid-port selection, guided-wave radiation, and the selection of a fixed subset from a planar grid have different feasible geometries, RF implementations, and switching constraints.

The communications literature also explores physical reconfiguration at several spatial and temporal scales. Two-timescale optimisation for movable-antenna systems [37] separates relatively slow position updates from faster transmit adaptation; multi-agent learning for movable-antenna-aided cell-free massive MIMO [38] applies mobility to distributed access points. Rotatable arrays for UAV mmWave MIMO [39] modify orientation, while joint precoding and morphing of flexible intelligent metasurfaces [40] changes the radiating structure. These methods are related to sparse-array optimisation through their additional spatial degrees of freedom, but their continuously or physically reconfigurable apertures do not impose the identical finite binary selection problem encountered with a hardware-limited non-uniform sparse array (NUSA).

2.8 Joint Beamforming, Sensing Accuracy, and Resource Allocation

In a shared ISAC transmitter, communication performance must be balanced against an estimation or detection objective. Joint beamforming and power allocation for full-duplex ISAC has been studied in [4], demonstrating the coupling between self-interference management and simultaneous sensing/communication processing. Optimal resource allocation for wideband ISAC [41] and energy-efficient hybrid beamfocusing for near-field ISAC [42] consider other relevant design dimensions: frequency selectivity, propagation regime, and energy cost. These results motivate a coupled rather than sequential resource-allocation approach, but they do not remove the added combinatorial difficulty when the active antenna positions must also be selected.

For parameter estimation, the Cramér–Rao bound (CRB) provides a principled link between beamformers, target responses, and the information available in noisy measurements. A CRB–rate trade-off for bistatic ISAC with Gaussian communication symbols and deterministic sensing signals is investigated in [43]; a related bistatic transceiver design directly targets CRB optimisation and explores learning-based solution methods [44]. These works are particularly

relevant to the present thesis because they explicitly distinguish communication utility from estimation accuracy rather than relying solely on beampattern sidelobes. Nevertheless, their bistatic observation models and signal assumptions need not yield the same Fisher information matrix as a common sparse planar transmit array. The CRB must therefore be derived for the thesis's own measurement model before it is introduced as an optimisation criterion.

Other joint design studies modify the propagation environment or receiver topology instead of the transmitter's physical antenna subset. Joint STAR-RIS-assisted ISAC design [45], robust STAR-RIS beamforming under hybrid-field propagation [46], and wideband cell-free STAR-RIS ISAC resource allocation [47] exploit additional reflecting/transmitting degrees of freedom. An overview of IRS-enabled sensing and communication [48] discusses architectures, limits, and joint beamforming considerations. Rate-splitting with RIS-assisted ISAC [49] and RIS-enabled secure radar–communication transmission [50] provide further instances of coupled communication and sensing constraints. Their optimisation structures are instructive, although adjusting a passive surface or multiple-access strategy is not equivalent to selecting which active transmit antennas and RF chains are present.

Security and system-level functionality create further competing demands. The MC-NOMA ISAC framework in [51] optimises communication and sensing security by combining tractable convex approximations with a global branch-and-bound benchmark, while a two-phase sensing-then-transmit framework [52] explicitly schedules secure sensing and transmission functions. In a broader setting, near-field multi-cell integrated sensing, communication, and powering (ISCAP) [53] and fluid-antenna LEO satellite systems supporting sensing, communication, and power transfer [54] show how spatial resources may serve more than two tasks. These studies demonstrate the breadth of ISAC resource allocation; the present thesis deliberately focuses on simultaneous multi-user downlink communication and target sensing, not security, energy transfer, or cross-cell coordination.

2.9 Implications for Non-Uniform Sparse ISAC Arrays

Taken together, the cited research identifies several modelling requirements for a hardware-constrained NUSA. First, the steering response should reflect the physical positions of the active elements and the assumed propagation regime, as indicated by near-field spatial-DoF and beamforming studies [13, 14]. Second, the communication metric must be calculated

using the same selected antenna set and transmit covariance that determine sensing accuracy; treating the rate and CRB as independent post-processing quantities could disguise the spatial competition between users and targets [43, 44]. Third, the number of active antennas (or RF chains) is an explicit design restriction, not merely a penalty added after continuous beamforming optimisation [23]. Finally, an alternating or relaxed optimisation framework must account for the discrete–continuous coupling rather than treating beamformer design and element activation as unrelated stages.

The scope of this thesis is consequently narrower than general reconfigurable-antenna or networked-ISAC optimisation but more integrated than prescribed-array beamforming: a single planar candidate grid is given, only a limited number of antenna positions can be activated, and communication sum rate, user QoS, and sensing CRB depend on the resulting common transmit signal. This scope makes it possible to isolate the value of non-uniform element selection while acknowledging that the design does not address mutual-coupling recalibration, beam training, mechanical movement, or time-varying channel acquisition.

2.10 Summary and Research Gap

The preceding literature can be organised along three complementary axes. Sparse-array and near-field MIMO studies show how aperture and element positions change spatial degrees of freedom and user discrimination [8, 13]. Radar-oriented sparse-array work connects element geometry to ambiguity, resolution, and implementation constraints [12, 30]. In parallel, ISAC transceiver, waveform, and surface-assisted studies jointly balance communication and sensing requirements, often with CRB-, rate-, or energy-based objectives [10, 41, 43, 45].

However, the approaches considered in this review leave a specific combination of decisions insufficiently addressed. A prescribed sparse aperture cannot exploit the freedom to select a non-uniform active set based on the users and targets currently served. Continuous-only beamforming schemes do not directly represent the on/off decision and cardinality limit imposed by an RF-chain budget. Finally, designing a sparse radar array from its aperture or beampattern alone does not ensure multi-user downlink quality of service when the sensing and communication functions share the same selected antenna positions and transmit power.

This thesis therefore studies the joint optimisation of a *binary non-uniform antenna activation pattern* and *continuous communication beamforming/resource variables* for a fixed candidate

planar grid, under user SINR, power, and active-chain constraints and with an explicit sensing CRB. Its central technical challenge is the coupling of a combinatorial geometric decision with non-convex communication–sensing performance measures. The resulting system model, objective, constraints, and optimisation approach are developed in Chapters 3 and 4 and the subsequent solution chapter. The claimed gap concerns this precise combination and should not be read as an assertion that prior ISAC studies have ignored sparse arrays, CRB optimisation, or antenna reconfiguration individually.

Chapter 3

System Model and Performance Metrics

3.1 System Architecture

Consider a millimetre-wave multi-user ISAC system operating in time-division-duplex mode. A dual-functional radar-communication base station (BS) serves K communication users while simultaneously sensing Q environmental targets. The carrier frequency and wavelength are denoted by f_c and λ_c, respectively. User k employs a UPA with $M_k = M_{x,k}M_{y,k}$ elements, whereas the BS contains a planar grid of $N = N_x N_y$ candidate transmit locations.

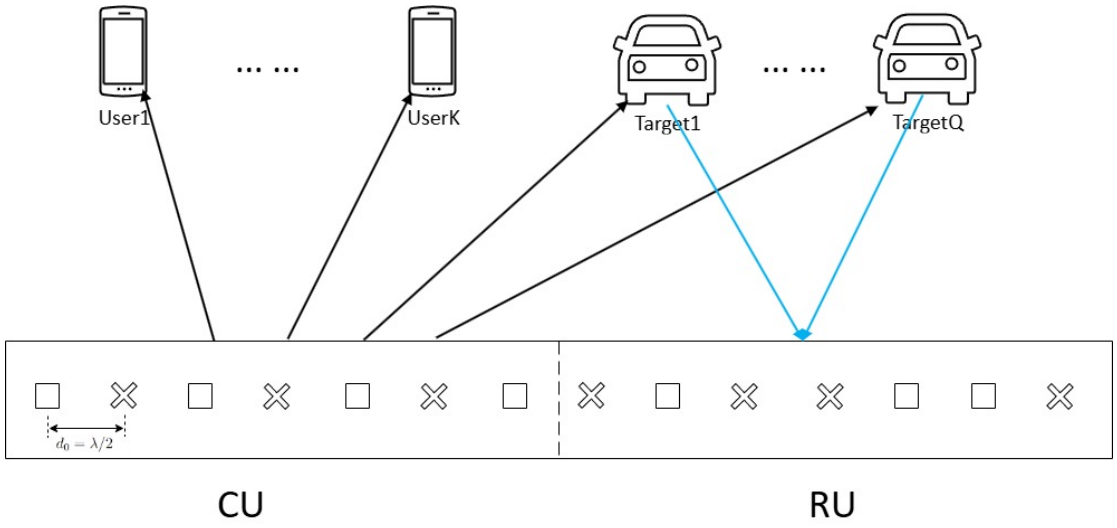

Figure 3.1: Multi-user ISAC system with dynamically selected communication-unit and radar-unit antenna elements.

In a conventional dense UPA, adjacent elements are separated by $\lambda_c/2$. A uniformly sparse array increases this spacing by a fixed integer factor, while a non-uniform sparse array uses irregular element locations. The latter provides more flexible spatial sampling and can balance

angular resolution, sidelobe behaviour, and hardware cost. To construct a dynamic NUSA from the full candidate grid, define

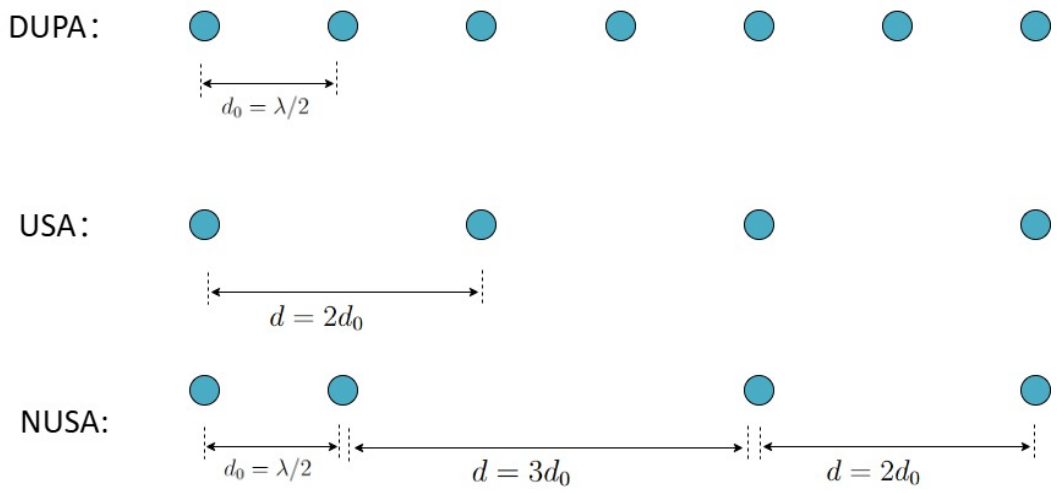

Figure 3.2: Illustration of dense, uniformly sparse, and non-uniformly sparse array layouts.

$$\boldsymbol{a} = [a_1, \ldots, a_N]^{\mathsf{T}}, \qquad \boldsymbol{D}_{\boldsymbol{a}} = \mathrm{diag}(\boldsymbol{a}), \qquad a_n \in \{0,1\}. \tag{3.1}$$

The value $a_n = 1$ indicates that candidate location n is connected to an RF chain; $a_n = 0$ removes that location from transmission. During each coherent interval, the communication signal also illuminates the targets, and the BS processes the reflected echoes for sensing. The user channels, target parameters, and activation pattern are assumed constant over this interval.

3.2 Array Response

Let $\boldsymbol{p}_n = [x_n, y_n, z_n]^{\mathsf{T}}$ denote candidate position n. For azimuth ϕ and elevation θ, the propagation-direction vector is

$$\boldsymbol{u}(\theta,\phi) = [\cos\theta\cos\phi, \cos\theta\sin\phi, \sin\theta]^{\mathsf{T}}. \tag{3.2}$$

The full-grid steering vector is

$$\boldsymbol{d}(\theta,\phi) = \frac{1}{\sqrt{N}}\left[e^{-j\frac{2\pi}{\lambda_c}\boldsymbol{p}_1^{\mathsf{T}}\boldsymbol{u}}, \ldots, e^{-j\frac{2\pi}{\lambda_c}\boldsymbol{p}_N^{\mathsf{T}}\boldsymbol{u}}\right]^{\mathsf{T}}. \tag{3.3}$$

For a half-wavelength-spaced $N_x \times N_y$ UPA, (3.3) reduces to

$$\boldsymbol{d}_t(\phi^{\mathrm{azi}}, \phi^{\mathrm{ele}}) = \boldsymbol{d}(\mu_\phi; N_x) \otimes \boldsymbol{d}(\nu_\phi; N_y), \tag{3.4}$$

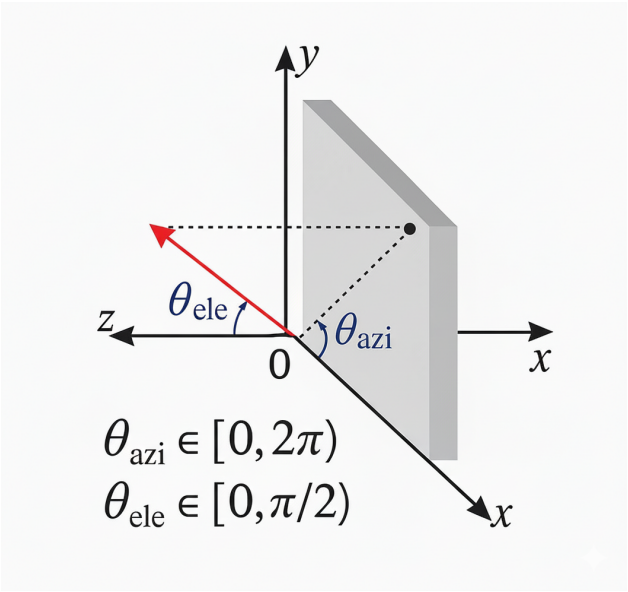

Figure 3.3: Azimuth and elevation angles for the planar-array coordinate system.

where

$$\mu_\phi = \cos\phi^{\text{azi}} \sin\phi^{\text{ele}}, \qquad \nu_\phi = \sin\phi^{\text{azi}} \sin\phi^{\text{ele}}, \tag{3.5}$$

and

$$\boldsymbol{d}(\mu; N_x) = \frac{1}{\sqrt{N_x}} [1, e^{-j\pi\mu}, \ldots, e^{-j\pi(N_x-1)\mu}]^{\mathsf{T}}. \tag{3.6}$$

The user-side receive steering vector $\boldsymbol{d}_r(\theta^{\text{azi}}, \theta^{\text{ele}})$ is defined analogously using $M_{x,k}$ and $M_{y,k}$. Antenna activation changes the BS response from $\boldsymbol{d}_t$ to $\boldsymbol{D}_{\boldsymbol{a}}\boldsymbol{d}_t$.

3.3 Communication Channel Model

The sparse mmWave channel model in [10] is adopted. The channel is quasi-static within a coherent processing interval and contains one line-of-sight path together with clustered non-line-of-sight paths:

$$\boldsymbol{H}_k(\tau) = \boldsymbol{H}_{k,\text{LoS}} p(\tau - \tau_{k,\text{LoS}}) + \sum_{c=1}^{N_C} \sum_{\ell=1}^{N_P} \boldsymbol{H}_{k,c,\ell} p(\tau - \tau_{k,c,\ell}), \tag{3.7}$$

where $p(\tau)$ is the pulse-shaping response, N_C is the number of scattering clusters, and N_P is the number of paths per cluster. The spatial channel associated with one path is

$$\boldsymbol{H}_{k,c,\ell} = g_{k,c,\ell} \boldsymbol{d}_r(\theta^{\text{azi}}_{k,c,\ell}, \theta^{\text{ele}}_{k,c,\ell}) \boldsymbol{d}_t^{\text{H}}(\phi^{\text{azi}}_{k,c,\ell}, \phi^{\text{ele}}_{k,c,\ell}), \tag{3.8}$$

where $g_{k,c,\ell}$ includes path loss and phase rotation. The narrowband equivalent channel used in the optimisation is denoted by $\boldsymbol{H}_k \in \mathbb{C}^{M_k \times N}$.

For target q, forward illumination and backward echo propagation form a monostatic radar channel. With L_q dominant reflection paths,

$$\boldsymbol{H}_{\mathrm{rad},q}(\tau) = \sum_{\ell=1}^{L_q} g_{q,\ell}\boldsymbol{d}_t(\theta_{q,\ell}^{\mathrm{azi}}, \theta_{q,\ell}^{\mathrm{ele}})\boldsymbol{d}_t^{\mathrm{H}}(\phi_{q,\ell}^{\mathrm{azi}}, \phi_{q,\ell}^{\mathrm{ele}})p(\tau - \tau_{q,\ell}), \tag{3.9}$$

where $g_{q,\ell}$ contains the target reflection coefficient and round-trip path loss. Since transmission and reception occur at the BS, $\boldsymbol{H}_{\mathrm{rad},q} \in \mathbb{C}^{N\times N}$.

3.4 Transmit and Received Signal Models

Let $s_k[t]$ denote the independent unit-power symbol intended for user k, i.e., $\mathbb{E}\{|s_k[t]|^2\} = 1$. The BS beamforming vector $\boldsymbol{w}_k \in \mathbb{C}^N$ includes both the spatial precoder and allocated signal amplitude. The common ISAC transmit vector is

$$\boldsymbol{x}[t] = \boldsymbol{D_a}\sum_{k=1}^{K} \boldsymbol{w}_k s_k[t]. \tag{3.10}$$

Thus, inactive elements are removed from the transmitted vector without modifying the physical channel definition. The corresponding covariance is

$$\boldsymbol{R}_x = \mathbb{E}\{\boldsymbol{x}[t]\boldsymbol{x}^{\mathrm{H}}[t]\} = \boldsymbol{D_a}\left(\sum_{k=1}^{K} \boldsymbol{w}_k\boldsymbol{w}_k^{\mathrm{H}}\right)\boldsymbol{D_a}. \tag{3.11}$$

For a frequency-selective channel with L taps, user k receives

$$\boldsymbol{y}_k[t] = \sum_{\ell=0}^{L-1} \boldsymbol{H}_k[\ell]\boldsymbol{x}[t-\ell] + \boldsymbol{n}_k[t], \tag{3.12}$$

where $\boldsymbol{n}_k[t] \sim \mathcal{CN}(\boldsymbol{0}, \sigma_k^2\boldsymbol{I})$. The BS simultaneously receives the target echoes

$$\boldsymbol{y}_{\mathrm{echo}}[t] = \sum_{q=1}^{Q}\sum_{\ell=0}^{L-1} \boldsymbol{H}_{\mathrm{rad},q}[\ell]\boldsymbol{x}[t-\ell] + \boldsymbol{n}_{\mathrm{BS}}[t], \tag{3.13}$$

where $\boldsymbol{n}_{\mathrm{BS}}[t] \sim \mathcal{CN}(\boldsymbol{0}, \sigma_{\mathrm{BS}}^2\boldsymbol{I})$.

3.5 Communication SINR and Achievable Rate

User k applies a linear combiner $\boldsymbol{v}_k \in \mathbb{C}^{M_k}$. For example, maximum-ratio combining uses the normalised receive steering vector in the dominant arrival direction. After combining, the

narrowband received signal is

$$y_k^{\text{out}}[t] = \underbrace{\boldsymbol{v}_k^{\text{H}} \boldsymbol{H}_k \boldsymbol{D}_{\boldsymbol{a}} \boldsymbol{w}_k s_k[t]}_{\text{desired signal}} + \underbrace{\sum_{i \neq k} \boldsymbol{v}_k^{\text{H}} \boldsymbol{H}_k \boldsymbol{D}_{\boldsymbol{a}} \boldsymbol{w}_i s_i[t]}_{\text{multi-user interference}} + \underbrace{\boldsymbol{v}_k^{\text{H}} \boldsymbol{n}_k[t]}_{\text{noise}}. \tag{3.14}$$

Define the effective channel $\boldsymbol{h}_k^{\text{H}} = \boldsymbol{v}_k^{\text{H}} \boldsymbol{H}_k$. Independence of the user symbols gives

$$\text{SINR}_k = \frac{|\boldsymbol{h}_k^{\text{H}} \boldsymbol{D}_{\boldsymbol{a}} \boldsymbol{w}_k|^2}{\sum_{i \neq k} |\boldsymbol{h}_k^{\text{H}} \boldsymbol{D}_{\boldsymbol{a}} \boldsymbol{w}_i|^2 + \sigma_k^2 \|\boldsymbol{v}_k\|_2^2}. \tag{3.15}$$

Assuming Gaussian signalling, the achievable communication sum rate is

$$U_{\text{comm}}(\boldsymbol{a}, \{\boldsymbol{w}_k\}) = \sum_{k=1}^{K} \log_2(1 + \text{SINR}_k). \tag{3.16}$$

3.6 Sensing SINR

To extract the echo of target q, the BS employs a receive beam $\boldsymbol{u}_q \in \mathbb{C}^N$ directed towards its estimated angle. Neglecting inter-symbol interference for clarity, the beamformer output is

$$\begin{aligned} y_q^{\text{echo}}[t] = &\sum_{i=1}^{K} \boldsymbol{u}_q^{\text{H}} \boldsymbol{H}_{\text{rad},q} \boldsymbol{D}_{\boldsymbol{a}} \boldsymbol{w}_i s_i[t] \\ &+ \sum_{r \neq q} \sum_{i=1}^{K} \boldsymbol{u}_q^{\text{H}} \boldsymbol{H}_{\text{rad},r} \boldsymbol{D}_{\boldsymbol{a}} \boldsymbol{w}_i s_i[t] + \boldsymbol{u}_q^{\text{H}} \boldsymbol{n}_{\text{BS}}[t]. \end{aligned} \tag{3.17}$$

The first term contains the desired echo, while the second contains echoes from other targets. The sensing SINR is therefore

$$\text{SINR}_q^{\text{sens}} = \frac{\sum_{i=1}^{K} |\boldsymbol{u}_q^{\text{H}} \boldsymbol{H}_{\text{rad},q} \boldsymbol{D}_{\boldsymbol{a}} \boldsymbol{w}_i|^2}{\sum_{r \neq q} \sum_{i=1}^{K} |\boldsymbol{u}_q^{\text{H}} \boldsymbol{H}_{\text{rad},r} \boldsymbol{D}_{\boldsymbol{a}} \boldsymbol{w}_i|^2 + \sigma_{\text{BS}}^2 \|\boldsymbol{u}_q\|_2^2}. \tag{3.18}$$

3.7 Fisher Information and Cramér–Rao Bound

For a dominant target path, collect the unknown reflection coefficient and angular parameters into

$$\boldsymbol{\eta}_q = [\Re\{g_q\}, \Im\{g_q\}, \theta_q^{\text{azi}}, \theta_q^{\text{ele}}, \phi_q^{\text{azi}}, \phi_q^{\text{ele}}]^{\mathsf{T}}. \tag{3.19}$$

After cancellation or suppression of the other target echoes, the mean observation at snapshot t is

$$\boldsymbol{\mu}_q[t; \boldsymbol{\eta}_q] = g_q \boldsymbol{d}_t(\theta_q^{\text{azi}}, \theta_q^{\text{ele}}) \boldsymbol{d}_t^{\text{H}}(\phi_q^{\text{azi}}, \phi_q^{\text{ele}}) \boldsymbol{x}[t]. \tag{3.20}$$

Stacking T snapshots gives a complex Gaussian observation with covariance $\sigma_{\mathrm{BS}}^2 \boldsymbol{I}$. The (m,n)-th FIM entry is [55]

$$[\boldsymbol{F}_q]_{m,n} = \frac{2}{\sigma_{\mathrm{BS}}^2} \Re\left\{ \sum_{t=0}^{T-1} \left(\frac{\partial \boldsymbol{\mu}_q[t]}{\partial \eta_{q,m}} \right)^{\mathrm{H}} \left(\frac{\partial \boldsymbol{\mu}_q[t]}{\partial \eta_{q,n}} \right) \right\}. \tag{3.21}$$

For example,

$$\frac{\partial \boldsymbol{\mu}_q[t]}{\partial \Re\{g_q\}} = \boldsymbol{d}_t(\theta_q^{\mathrm{azi}}, \theta_q^{\mathrm{ele}}) c_q[t], \tag{3.22}$$

$$\frac{\partial \boldsymbol{\mu}_q[t]}{\partial \Im\{g_q\}} = j\boldsymbol{d}_t(\theta_q^{\mathrm{azi}}, \theta_q^{\mathrm{ele}}) c_q[t], \tag{3.23}$$

$$\frac{\partial \boldsymbol{\mu}_q[t]}{\partial \theta_q^{\mathrm{azi}}} = g_q \frac{\partial \boldsymbol{d}_t(\theta_q^{\mathrm{azi}}, \theta_q^{\mathrm{ele}})}{\partial \theta_q^{\mathrm{azi}}} c_q[t], \tag{3.24}$$

where

$$c_q[t] = \boldsymbol{d}_t^{\mathrm{H}}(\phi_q^{\mathrm{azi}}, \phi_q^{\mathrm{ele}}) \boldsymbol{x}[t]. \tag{3.25}$$

The remaining derivatives follow analogously. Since $\boldsymbol{x}[t]$ contains $\boldsymbol{D_a}$ and $\{\boldsymbol{w}_k\}$, the FIM depends directly on both the selected aperture and transmit beamforming.

For any unbiased estimator,

$$\mathrm{Cov}(\widehat{\boldsymbol{\eta}}_q) \succeq \boldsymbol{F}_q^{-1}, \qquad \mathrm{Var}(\widehat{\eta}_{q,p}) \geq [\boldsymbol{F}_q^{-1}]_{p,p}. \tag{3.26}$$

A scalar sensing cost is obtained by weighting the parameters of interest:

$$J_{\mathrm{sense}}(\boldsymbol{a}, \{\boldsymbol{w}_k\}) = \sum_{q=1}^{Q} \mathrm{tr}\left(\boldsymbol{\Omega}_q \boldsymbol{F}_q^{-1} \right), \tag{3.27}$$

where $\boldsymbol{\Omega}_q \succeq \boldsymbol{0}$. A lower value corresponds to a tighter estimation-error bound. The CRB decreases when the sensing SNR increases, the target illumination becomes stronger, or the active geometry produces steering-vector derivatives with larger norms.

3.8 Modelling Assumptions

Channel and target parameters are assumed known at the beginning of each design interval and remain constant during optimisation. The array is calibrated, switching is ideal, and the noise processes are spatially white. Inter-target echoes are assumed separable or treated as nuisance parameters in the FIM. Mutual coupling, switching transients, channel-estimation overhead, and robustness to imperfect parameter information are outside the present optimisation model and will be considered when interpreting the numerical results.

Chapter 4

Joint Optimisation Problem Formulation

4.1 Joint Design Formulation

The non-uniform antenna activation pattern and the multi-user transmit beamformers are jointly designed to maximise the achievable communication sum rate while improving the target-parameter estimation accuracy. Meanwhile, the prescribed communication quality of service (QoS), the available transmit-power budget, and the limited number of RF chains must be guaranteed. Accordingly, the joint sparse-array selection and beamforming design for the considered ISAC system is formulated as

$$\mathcal{P}_0: \quad \underset{\boldsymbol{a},\{\boldsymbol{w}_k\}}{\text{maximize}} \quad U_{\text{comm}}(\boldsymbol{a},\{\boldsymbol{w}_k\}) - \lambda J_{\text{sense}}(\boldsymbol{a},\{\boldsymbol{w}_k\}) \tag{4.1a}$$

$$\text{subject to} \quad \text{SINR}_k(\boldsymbol{a},\{\boldsymbol{w}_i\}) \geq \gamma_k, \quad k=1,\ldots,K, \tag{C1}$$

$$\sum_{k=1}^{K} \|\boldsymbol{D}_{\boldsymbol{a}}\boldsymbol{w}_k\|_2^2 \leq P_{\max}, \tag{C2}$$

$$\mathbf{1}^{\mathsf{T}}\boldsymbol{a} \leq S_{\max}, \tag{C3}$$

$$a_n \in \{0,1\}, \quad n=1,\ldots,N. \tag{C4}$$

where the non-negative coefficient λ controls the relative priority assigned to communication and sensing. The minimum SINR requirement of each communication user is specified by C1. Constraint C2 limits the total power radiated through the selected antenna elements. Moreover, the RF-chain budget is imposed by C3, which allows no more than $S_{\max}$ candidate locations to be activated. The binary switching behaviour is prescribed by C4. Constraints C3 and C4 jointly ensure that the resulting NUSA layout can be implemented by the antenna switch network.

4.2 Objective-Function Expansion and Convexity

According to (3.16) and (3.27), substituting the communication SINR in (3.15) and the transmit covariance in (3.11) into (4.1a) yields

$$O(\boldsymbol{a},\{\boldsymbol{w}_i\}) = \sum_{k=1}^{K} \log_2 \left(1 + \frac{\left| \sum_{n=1}^{N} a_n h_{k,n}^{*} w_{k,n} \right|^2}{\sum_{i \neq k} \left| \sum_{n=1}^{N} a_n h_{k,n}^{*} w_{i,n} \right|^2 + \nu_k} \right) - \lambda \sum_{q=1}^{Q} \operatorname{tr}\left(\boldsymbol{\Omega}_q \widetilde{\boldsymbol{F}}_q^{-1}(\boldsymbol{a},\{\boldsymbol{w}_i\}) \right), \tag{4.2}$$

where $\nu_k = \sigma_k^2 \|\boldsymbol{v}_k\|_2^2$. For the linear Gaussian sensing model, the (r,s)-th entry of $\widetilde{\boldsymbol{F}}_q$ is

$$[\widetilde{\boldsymbol{F}}_q]_{r,s} = \operatorname{tr}\left(\boldsymbol{B}_{q,r,s} \boldsymbol{D}_{\boldsymbol{a}} \left(\sum_{i=1}^{K} \boldsymbol{w}_i \boldsymbol{w}_i^{\mathrm{H}} \right) \boldsymbol{D}_{\boldsymbol{a}} \right) \tag{4.3}$$

$$= \sum_{n=1}^{N} \sum_{m=1}^{N} a_n a_m \left(\sum_{i=1}^{K} w_{i,n} w_{i,m}^{*} \right) [\boldsymbol{B}_{q,r,s}]_{m,n}. \tag{4.4}$$

The coefficient matrix $\boldsymbol{B}_{q,r,s}$ is determined by the target response, the array-manifold derivatives, and the sensing-noise covariance.

To reveal the difference structure of the communication utility, define

$$T_k(\boldsymbol{a},\{\boldsymbol{w}_i\}) = \sum_{i=1}^{K} \left| \sum_{n=1}^{N} a_n h_{k,n}^{*} w_{i,n} \right|^2 + \nu_k, \tag{4.5}$$

$$I_k(\boldsymbol{a},\{\boldsymbol{w}_i\}) = \sum_{i \neq k} \left| \sum_{n=1}^{N} a_n h_{k,n}^{*} w_{i,n} \right|^2 + \nu_k. \tag{4.6}$$

Since $1 + \mathrm{SINR}_k = T_k / I_k$, (3.16) is equivalently expressed as

$$U_{\mathrm{comm}} = \sum_{k=1}^{K} \left[\log_2 T_k - \log_2 I_k \right]. \tag{4.7}$$

For a fixed activation vector and the lifted beamforming matrices $\boldsymbol{W}_i = \boldsymbol{w}_i \boldsymbol{w}_i^{\mathrm{H}}$, both T_k and I_k are positive affine functions of $\{\boldsymbol{W}_i\}$. Consequently, $\log_2 T_k$ and $\log_2 I_k$ are concave in the lifted beamforming variables. Their difference in (4.7), however, is not concave. For the original joint variables, the terms T_k and I_k contain $a_n a_m w_{i,n} w_{i,m}^{*}$ and are neither convex nor concave, which further confirms the joint non-convexity of the communication utility.

Similarly, (3.27) and (4.4) give

$$J_{\mathrm{sense}} = sum_{q=1}^{Q} \operatorname{tr}\left(\boldsymbol{\Omega}_q \widetilde{\boldsymbol{F}}_q^{-1}(\boldsymbol{a},\{\boldsymbol{w}_i\}) \right). \tag{4.8}$$

The mapping $\boldsymbol{F} \mapsto \mathrm{tr}(\boldsymbol{\Omega}_q \boldsymbol{F}^{-1})$ is convex over the positive-definite cone for $\boldsymbol{\Omega}_q \succeq \mathbf{0}$. Hence, for a fixed array geometry and lifted beamforming matrices, J_{sense} is convex because $\widetilde{\boldsymbol{F}}_q$ is affine in $\{\boldsymbol{W}_i\}$. In the original joint variables, however, (4.4) contains the products $a_n a_m w_{i,n} w_{i,m}^*$; therefore, the mapping from $(\boldsymbol{a}, \{\boldsymbol{w}_i\})$ to $\widetilde{\boldsymbol{F}}_q$ is non-affine and J_{sense} is not jointly convex.

Using (4.7) and (4.8), the objective in (4.1a) can finally be written as

$$O = \underbrace{\sum_{k=1}^{K} \log_2 T_k}_{\text{concave after block lifting}} - \underbrace{\sum_{k=1}^{K} \log_2 I_k}_{\text{concave after block lifting}} - \lambda \underbrace{\sum_{q=1}^{Q} \mathrm{tr}\left(\boldsymbol{\Omega}_q \widetilde{\boldsymbol{F}}_q^{-1}\right)}_{\text{convex after block lifting}} . \tag{4.9}$$

The subtraction of the concave interference term prevents (4.9) from being concave even after one variable block is fixed and lifted. Moreover, the multiplicative coupling in the original variables renders the complete objective jointly non-convex.

For later use, define

$$\boldsymbol{c}_{k,i} = \mathrm{diag}(\boldsymbol{h}_k^*)\boldsymbol{w}_i, \qquad \boldsymbol{C}_{k,i} = \boldsymbol{c}_{k,i}\boldsymbol{c}_{k,i}^{\mathrm{H}} \succeq \mathbf{0}. \tag{4.10}$$

The received amplitude and power can then be represented as

$$\boldsymbol{h}_k^{\mathrm{H}} \boldsymbol{D}_{\boldsymbol{a}} \boldsymbol{w}_i = \boldsymbol{a}^{\mathsf{T}} \boldsymbol{c}_{k,i}, \tag{4.11}$$

$$|\boldsymbol{h}_k^{\mathrm{H}} \boldsymbol{D}_{\boldsymbol{a}} \boldsymbol{w}_i|^2 = \boldsymbol{a}^{\mathsf{T}} \boldsymbol{C}_{k,i} \boldsymbol{a}. \tag{4.12}$$

Accordingly,

$$\mathrm{SINR}_k = \frac{\boldsymbol{a}^{\mathsf{T}} \boldsymbol{C}_{k,k} \boldsymbol{a}}{\sum_{i \neq k} \boldsymbol{a}^{\mathsf{T}} \boldsymbol{C}_{k,i} \boldsymbol{a} + \nu_k}. \tag{4.13}$$

4.3 Convexity Analysis and Constraint Reformulation

Substituting (4.13) into C1 and multiplying both sides by the strictly positive interference-plus-noise denominator gives

$$\gamma_k \sum_{i \neq k} \boldsymbol{a}^{\mathsf{T}} \boldsymbol{C}_{k,i} \boldsymbol{a} + \gamma_k \nu_k - \boldsymbol{a}^{\mathsf{T}} \boldsymbol{C}_{k,k} \boldsymbol{a} \leq 0. \tag{4.14}$$

For fixed beamformers, each quadratic form $\boldsymbol{a}^{\mathsf{T}} \boldsymbol{C}_{k,i} \boldsymbol{a}$ is convex because $\boldsymbol{C}_{k,i} \succeq \mathbf{0}$. Nevertheless, the desired-signal term appears with a negative sign, and C1 is therefore a difference-of-convex constraint. For a fixed activation vector, the interference and desired-signal powers are also convex quadratic functions of the beamformers, with the desired term subtracted. Thus, C1 remains non-convex before matrix lifting.

Constraint C2 can be expanded as

$$\sum_{k=1}^{K} \|\boldsymbol{D}_{\boldsymbol{a}} \boldsymbol{w}_k\|_2^2 = \sum_{k=1}^{K} \sum_{n=1}^{N} a_n^2 |w_{k,n}|^2 \tag{4.15}$$

$$= \sum_{n=1}^{N} a_n \left(\sum_{k=1}^{K} |w_{k,n}|^2 \right) \leq P_{\max}, \tag{4.16}$$

where the equality $a_n^2 = a_n$ follows from C4. For fixed $\boldsymbol{a}$, C2 is a convex quadratic constraint in the beamformers. For fixed beamformers, it is affine in $\boldsymbol{a}$. The product $a_n |w_{k,n}|^2$, however, is not jointly convex over the relaxed domain $0 \leq a_n \leq 1$.

Under C4, the active-antenna limit in C3 is equivalently written as

$$\sum_{n=1}^{N} a_n = \mathbf{1}^{\mathsf{T}} \boldsymbol{a} \leq S_{\max}. \tag{4.17}$$

This inequality is affine. Its combinatorial difficulty arises from the binary domain imposed by C4 rather than from C3 itself.

The feasible set $\{0,1\}^N$ specified by C4 is non-convex. Its continuous relaxation is

$$0 \leq a_n \leq 1. \tag{4.18}$$

Although (4.18) defines a convex box, a solution in this relaxed set can contain fractional entries and cannot be implemented directly by the antenna switches. A subsequent rank-one relaxation and binary-recovery procedure is therefore required.

4.4 Reformulation Strategy

Despite the equivalent transformations above, problem (4.1) remains non-convex. In particular, the communication utility in (4.7) is expressed as the difference of two concave logarithmic terms and is therefore not jointly concave. Constraint C1 in (4.14) contains a negative desired-signal quadratic term, whereas (4.4) and (4.16) retain the multiplicative coupling between the activation and beamforming variables. In addition, the inverse FIM and the discrete feasible set in C4 prevent the direct application of standard convex optimisation methods.

In the sequel, these difficulties are handled in a prescribed order. First, the antenna activation and beamforming variables are separated through an alternating-optimisation framework. For a given antenna layout, the beamforming outer products $\boldsymbol{W}_k = \boldsymbol{w}_k \boldsymbol{w}_k^{\mathrm{H}}$ are introduced so that the received powers and FIM become affine functions of $\{\boldsymbol{W}_k\}$. The resulting rank-one constraints

are treated by semidefinite relaxation (SDR) [56]. Similarly, for given beamformers, the activation outer product $\boldsymbol{A} = \boldsymbol{a}\boldsymbol{a}^{\mathsf{T}}$ is introduced, and its rank-one condition is relaxed to obtain a semidefinite representation of the array-selection problem.

After these matrix-lifting operations, the QoS, power, and CRB constraints can be represented by affine inequalities or linear matrix inequalities. Nevertheless, the difference-of-logarithms structure of the communication objective remains non-concave. Successive convex approximation (SCA) is therefore employed to replace the subtracted logarithmic term by its first-order affine upper bound at the current feasible point. This construction yields a concave lower-bound objective that is locally tight and gradient consistent [57]. Similar combinations of semidefinite reformulation and SCA have been employed to handle coupled beamforming and resource-allocation variables in non-convex ISAC optimisation problems [51].

SDR is not assumed to be universally tight for the joint ISAC design considered here. When a relaxed matrix is rank one, the corresponding physical vector is recovered exactly. Otherwise, a rank-one candidate is generated through eigenvector extraction or Gaussian randomisation and is subsequently checked against the original constraints. Accordingly, the proposed procedure provides a low-complexity suboptimal solution rather than a claim of global optimality. The detailed block-wise transformations and the resulting convex subproblems are presented in Chapter 5.

Chapter 5

Low-Complexity Suboptimal Solution

5.1 Alternating-Optimisation Framework

In this chapter, a low-complexity suboptimal scheme is developed for solving (4.1). As shown in Chapter 4, the antenna activation vector and the user beamformers are tightly coupled in the communication powers, transmit covariance, and sensing FIM. Directly optimising the two variable groups is therefore computationally intractable. To decouple them, we adopt an alternating-optimisation (AO) framework. Specifically, for the r-th outer iteration, the sparse layout $\boldsymbol{a}^{(r)}$ is first fixed and the transmit beamformers are updated. The newly obtained beamformers are then fixed while the antenna activation pattern is redesigned. These two steps are executed successively until the original feasible objective satisfies the convergence criterion.

The conditional problems are still non-convex. The beamforming update contains rank-one covariance constraints and a difference-of-logarithms objective, whereas the array update contains quadratic binary products and the same non-concave rate structure. We therefore combine SDR with SCA in both blocks, as detailed below.

5.2 Subproblem 1: Transmit Beamforming Design

5.2.1 Fixed-array quantities and matrix lifting

To begin with, we fix the antenna activation vector as $\boldsymbol{a} = \boldsymbol{a}^{(r)}$. In this case, the array geometry and effective user channels are known constants. Define

$$\bar{\boldsymbol{h}}_k = \boldsymbol{D}_{\boldsymbol{a}^{(r)}} \boldsymbol{h}_k, \qquad \bar{\boldsymbol{H}}_k = \bar{\boldsymbol{h}}_k \bar{\boldsymbol{h}}_k^{\mathrm{H}} \succeq \boldsymbol{0}. \tag{5.1}$$

The received power from stream i becomes

$$|\boldsymbol{h}_k^{\mathrm{H}} \boldsymbol{D}_{\boldsymbol{a}^{(r)}} \boldsymbol{w}_i|^2 = \boldsymbol{w}_i^{\mathrm{H}} \overline{\boldsymbol{H}}_k \boldsymbol{w}_i. \tag{5.2}$$

Introduce the lifted beamforming matrix

$$\boldsymbol{W}_i = \boldsymbol{w}_i \boldsymbol{w}_i^{\mathrm{H}}, \qquad \boldsymbol{W}_i \succeq \boldsymbol{0}, \qquad \operatorname{rank}(\boldsymbol{W}_i) = 1. \tag{5.3}$$

Using $\boldsymbol{x}^{\mathrm{H}} \boldsymbol{B} \boldsymbol{x} = \operatorname{tr}(\boldsymbol{B} \boldsymbol{x} \boldsymbol{x}^{\mathrm{H}})$, (5.2) becomes the affine expression

$$|\boldsymbol{h}_k^{\mathrm{H}} \boldsymbol{D}_{\boldsymbol{a}^{(r)}} \boldsymbol{w}_i|^2 = \operatorname{tr}(\overline{\boldsymbol{H}}_k \boldsymbol{W}_i). \tag{5.4}$$

5.2.2 Transformation of C1

For a fixed array, C1 is

$$\frac{\operatorname{tr}(\overline{\boldsymbol{H}}_k \boldsymbol{W}_k)}{\sum_{i \neq k} \operatorname{tr}(\overline{\boldsymbol{H}}_k \boldsymbol{W}_i) + \nu_k} \geq \gamma_k. \tag{5.5}$$

Multiplication by the positive denominator gives

$$\operatorname{tr}(\overline{\boldsymbol{H}}_k \boldsymbol{W}_k) - \gamma_k \sum_{i \neq k} \operatorname{tr}(\overline{\boldsymbol{H}}_k \boldsymbol{W}_i) \geq \gamma_k \nu_k. \tag{5.6}$$

Every term in (5.6) is affine in $\{\boldsymbol{W}_i\}$. Thus, the apparently non-convex SINR constraint becomes a linear inequality after lifting. The remaining difficulty is the rank-one condition in (5.3), not C1 itself.

5.2.3 Transformation of C2–C4

Because the activation matrix is fixed, C2 becomes

$$\begin{aligned} \sum_{i=1}^{K} \|\boldsymbol{D}_{\boldsymbol{a}^{(r)}} \boldsymbol{w}_i\|_2^2 &= \sum_{i=1}^{K} \operatorname{tr}(\boldsymbol{D}_{\boldsymbol{a}^{(r)}} \boldsymbol{W}_i \boldsymbol{D}_{\boldsymbol{a}^{(r)}}) \\ &= \sum_{i=1}^{K} \operatorname{tr}(\boldsymbol{D}_{\boldsymbol{a}^{(r)}} \boldsymbol{W}_i) \leq P_{\max}, \end{aligned} \tag{5.7}$$

where $(\boldsymbol{D}_{\boldsymbol{a}^{(r)}})^2 = \boldsymbol{D}_{\boldsymbol{a}^{(r)}}$ for a binary vector. Equation (5.7) is affine in the lifted matrices. C3 and C4 are already satisfied by the fixed feasible vector $\boldsymbol{a}^{(r)}$ and therefore do not appear as optimisation constraints in Subproblem 1.

5.2.4 SCA transformation of the communication objective

Define

$$\mathcal{T}_k(\{\boldsymbol{W}_i\}) = \sum_{i=1}^{K} \mathrm{tr}(\overline{\boldsymbol{H}}_k \boldsymbol{W}_i) + \nu_k, \tag{5.8}$$

$$I_k(\{\boldsymbol{W}_i\}) = \sum_{i \neq k} \mathrm{tr}(\overline{\boldsymbol{H}}_k \boldsymbol{W}_i) + \nu_k. \tag{5.9}$$

Both are positive affine functions. Hence

$$R_k = \underbrace{\log_2 \mathcal{T}_k}_{f_k(\boldsymbol{W})} - \underbrace{\log_2 I_k}_{g_k(\boldsymbol{W})}. \tag{5.10}$$

Both f_k and g_k are concave. Their difference is generally neither concave nor convex. For a maximisation problem, SCA constructs a concave lower bound by replacing the subtracted concave function g_k with its global affine upper bound. At inner iteration t, concavity gives

$$\begin{aligned} g_k(\boldsymbol{W}) &\leq \widehat{g}_k^{(t)}(\boldsymbol{W}) \\ &= \log_2 I_k^{(t)} + \frac{I_k(\boldsymbol{W}) - I_k^{(t)}}{\ln(2)\, I_k^{(t)}}, \end{aligned} \tag{5.11}$$

where $I_k^{(t)} = I_k(\{\boldsymbol{W}_i^{(t)}\})$. Therefore

$$R_k \geq \widehat{R}_k^{(t)} = \log_2 \mathcal{T}_k - \widehat{g}_k^{(t)}. \tag{5.12}$$

The lower bound is concave, equals the original rate at the expansion point, and has the same gradient there.

5.2.5 Transformation of the sensing objective

With the array fixed, the active transmit covariance is

$$\boldsymbol{R}_x = \boldsymbol{D}_{\boldsymbol{a}^{(r)}} \left(\sum_{i=1}^{K} \boldsymbol{W}_i \right) \boldsymbol{D}_{\boldsymbol{a}^{(r)}}. \tag{5.13}$$

Substitution into (4.3) shows that every FIM entry is affine in $\{\boldsymbol{W}_i\}$:

$$[\boldsymbol{F}_q(\boldsymbol{W})]_{u,v} = \sum_{i=1}^{K} \mathrm{tr}\left(\boldsymbol{D}_{\boldsymbol{a}^{(r)}} \boldsymbol{B}_{q,u,v} \boldsymbol{D}_{\boldsymbol{a}^{(r)}} \boldsymbol{W}_i \right). \tag{5.14}$$

Introduce $\boldsymbol{Y}_q \succeq \boldsymbol{0}$ and require $\boldsymbol{Y}_q \succeq \boldsymbol{F}_q^{-1}$. By the Schur complement,

$$\begin{bmatrix} \boldsymbol{Y}_q & \boldsymbol{I} \\ \boldsymbol{I} & \boldsymbol{F}_q(\boldsymbol{W}) \end{bmatrix} \succeq \boldsymbol{0}. \tag{5.15}$$

The sensing cost is then replaced by the linear epigraph objective $\sum_q \mathrm{tr}(\boldsymbol{\Omega}_q \boldsymbol{Y}_q)$. Because the maximisation objective contains its negative, the term $-\lambda \sum_q \mathrm{tr}(\boldsymbol{\Omega}_q \boldsymbol{Y}_q)$ is affine and concave.

5.2.6 Resulting beamforming subproblem

Given the current SCA expansion point, we first handle the non-convexity introduced by the rank-one conditions in (5.3) through SDR and remove these conditions from the feasible set. By combining (5.6), (5.7), (5.15), and the concave rate lower bound (5.12), the beamforming update is recast as

$$\mathcal{P}_{\mathrm{BF}}^{(t)}: \quad \underset{\{\boldsymbol{W}_i\},\{\boldsymbol{Y}_q\}}{\text{maximize}} \quad \sum_{k=1}^{K} \widehat{R}_k^{(t)} - \lambda \sum_{q=1}^{Q} \mathrm{tr}(\boldsymbol{\Omega}_q \boldsymbol{Y}_q) \tag{5.16a}$$

$$\text{subject to} \quad (5.6), \quad k = 1,\ldots,K, \tag{5.16b}$$

$$(5.7), \tag{5.16c}$$

$$(5.15), \quad q = 1,\ldots,Q, \tag{5.16d}$$

$$\boldsymbol{W}_i \succeq \boldsymbol{0}, \quad i = 1,\ldots,K. \tag{5.16e}$$

Problem (5.16) has a concave objective and contains only affine constraints and LMIs. It is therefore a convex SDP and can be efficiently solved using a standard interior-point solver through CVX [58]. Since the tangent approximation depends on the current point, (5.16) is solved iteratively. After each solution, $I_k^{(t)}$ is updated and a new affine upper bound is constructed until the relative change of the inner objective falls below the prescribed tolerance.

The SDR step drops $\mathrm{rank}(\boldsymbol{W}_i) = 1$. If the optimal $\boldsymbol{W}_i^\star$ is rank one, the beamformer is obtained from its principal eigenpair. If it has higher rank, Gaussian randomisation or a rank-reduction procedure is used, followed by a power/QoS feasibility check. The objective must subsequently be evaluated using the recovered beamforming vectors rather than only the relaxed matrices.

5.3 Subproblem 2: Non-Uniform Antenna Selection

5.3.1 Quadratic activation form and lifting

We next fix the transmit beamformers as $\boldsymbol{w}_i = \boldsymbol{w}_i^{(r+1)}$ and optimise the NUSA layout. Under the fixed beamforming strategy, the vectors $\boldsymbol{c}_{k,i}$ and matrices $\boldsymbol{C}_{k,i}$ in (4.10) are constants. Nevertheless, (4.12) still contains the quadratic product $\boldsymbol{a}\boldsymbol{a}^{\mathsf{T}}$. To expose this coupling, we introduce

$$\boldsymbol{A} = \boldsymbol{a}\boldsymbol{a}^{\mathsf{T}}, \qquad \boldsymbol{A} \succeq \boldsymbol{0}, \qquad \mathrm{rank}(\boldsymbol{A}) = 1. \tag{5.17}$$

Then

$$\boldsymbol{a}^{\mathsf{T}} \boldsymbol{C}_{k,i} \boldsymbol{a} = \mathrm{tr}(\boldsymbol{C}_{k,i} \boldsymbol{A}), \tag{5.18}$$

which is affine in $\boldsymbol{A}$.

For a binary vector, $a_n^2 = a_n$, so the exact lifted variables satisfy

$$\operatorname{diag}(\boldsymbol{A}) = \boldsymbol{a}. \tag{5.19}$$

The equality $\boldsymbol{A} = \boldsymbol{a}\boldsymbol{a}^{\mathsf{T}}$ is equivalently characterised by the Schur matrix and a rank-one condition:

$$\begin{bmatrix} \boldsymbol{A} & \boldsymbol{a} \\ \boldsymbol{a}^{\mathsf{T}} & 1 \end{bmatrix} \succeq \mathbf{0}, \qquad \operatorname{rank} \begin{bmatrix} \boldsymbol{A} & \boldsymbol{a} \\ \boldsymbol{a}^{\mathsf{T}} & 1 \end{bmatrix} = 1. \tag{5.20}$$

SDR removes the rank condition and retains the LMI, (5.19), and $0 \le a_n \le 1$.

5.3.2 Transformation of C1

Using (5.18), the QoS constraint (4.14) becomes

$$\operatorname{tr}(\boldsymbol{C}_{k,k}\boldsymbol{A}) - \gamma_k \sum_{i \neq k} \operatorname{tr}(\boldsymbol{C}_{k,i}\boldsymbol{A}) \ge \gamma_k \nu_k. \tag{5.21}$$

This is affine in $\boldsymbol{A}$. Lifting therefore removes the difference-of-quadratic structure of C1; the relaxation error is isolated in the dropped rank-one/binary conditions.

5.3.3 Transformation of C2–C4

For the fixed beamformers, define the power used at candidate location n as

$$p_n = \sum_{i=1}^{K} |w_{i,n}^{(r+1)}|^2, \qquad \boldsymbol{P} = \operatorname{diag}(p_1, \ldots, p_N). \tag{5.22}$$

From (4.15), C2 becomes

$$\sum_{n=1}^{N} p_n A_{n,n} = \operatorname{tr}(\boldsymbol{P}\boldsymbol{A}) \le P_{\max}. \tag{5.23}$$

C3 and the relaxed C4 are

$$\mathbf{1}^{\mathsf{T}}\boldsymbol{a} \le S_{\max}, \qquad 0 \le a_n \le 1. \tag{5.24}$$

Together with (5.19) and the relaxed version of (5.20), these constraints form a convex feasible set.

5.3.4 SCA transformation of the communication objective

For fixed beamformers, define

$$\mathcal{T}_k(\boldsymbol{A}) = \sum_{i=1}^{K} \operatorname{tr}(\boldsymbol{C}_{k,i}\boldsymbol{A}) + \nu_k, \tag{5.25}$$

$$I_k(\boldsymbol{A}) = \sum_{i\neq k} \operatorname{tr}(\boldsymbol{C}_{k,i}\boldsymbol{A}) + \nu_k. \tag{5.26}$$

The user rate is again a difference of concave logarithms:

$$R_k(\boldsymbol{A}) = \log_2 \mathcal{T}_k(\boldsymbol{A}) - \log_2 I_k(\boldsymbol{A}). \tag{5.27}$$

At SCA iteration t, the second logarithm obeys

$$\begin{aligned}\log_2 I_k(\boldsymbol{A}) \leq\ & \log_2 I_k(\boldsymbol{A}^{(t)}) \\ & + \frac{I_k(\boldsymbol{A}) - I_k(\boldsymbol{A}^{(t)})}{\ln(2)\, I_k(\boldsymbol{A}^{(t)})}.\end{aligned} \tag{5.28}$$

Denote this affine upper bound by $\widehat{g}_{k,A}^{(t)}(\boldsymbol{A})$. A concave lower bound on the rate is

$$\widehat{R}_{k,A}^{(t)}(\boldsymbol{A}) = \log_2 \mathcal{T}_k(\boldsymbol{A}) - \widehat{g}_{k,A}^{(t)}(\boldsymbol{A}). \tag{5.29}$$

5.3.5 Transformation of the sensing objective

With fixed $\boldsymbol{W} = \sum_i \boldsymbol{w}_i \boldsymbol{w}_i^{\mathrm{H}}$, define

$$[\boldsymbol{G}_{q,u,v}]_{n,m} = [\boldsymbol{W}]_{n,m}[\boldsymbol{B}_{q,u,v}]_{m,n}. \tag{5.30}$$

Equation (4.4) becomes

$$[\boldsymbol{F}_q(\boldsymbol{A})]_{u,v} = \operatorname{tr}(\boldsymbol{G}_{q,u,v}^{\mathsf{T}}\boldsymbol{A}), \tag{5.31}$$

which is affine in $\boldsymbol{A}$. The inverse is removed using

$$\begin{bmatrix} \boldsymbol{Y}_q & \boldsymbol{I} \\ \boldsymbol{I} & \boldsymbol{F}_q(\boldsymbol{A}) \end{bmatrix} \succeq \boldsymbol{0}. \tag{5.32}$$

5.3.6 Resulting antenna-selection subproblem

We first relax the continuous rank-one condition in (5.20) by applying SDR. Then, for a given SCA point $\boldsymbol{A}^{(t)}$, we substitute the concave lower bound (5.29) and the LMI representation (5.32).

Consequently, the antenna-selection problem is transformed into

$$\mathcal{P}_{\mathrm{AS}}^{(t)}: \quad \underset{\boldsymbol{A},\boldsymbol{a},\{\boldsymbol{Y}_q\}}{\text{maximize}} \quad \sum_{k=1}^{K} \widehat{R}_{k,A}^{(t)}(\boldsymbol{A}) - \lambda \sum_{q=1}^{Q} \mathrm{tr}(\boldsymbol{\Omega}_q \boldsymbol{Y}_q) \tag{5.33a}$$

$$\text{subject to} \quad (5.21), \quad k = 1,\ldots,K, \tag{5.33b}$$

$$(5.23), \quad (5.24), \tag{5.33c}$$

$$\mathrm{diag}(\boldsymbol{A}) = \boldsymbol{a}, \tag{5.33d}$$

$$\begin{bmatrix} \boldsymbol{A} & \boldsymbol{a} \\ \boldsymbol{a}^{\mathsf{T}} & 1 \end{bmatrix} \succeq \boldsymbol{0}, \tag{5.33e}$$

$$(5.32), \quad q = 1,\ldots,Q. \tag{5.33f}$$

Problem (5.33) has a concave objective over a convex semidefinite feasible set and can also be solved efficiently by CVX. The SCA point is updated iteratively until convergence. It is worth noting that the solution of (5.33) belongs to the relaxed feasible set. Hence, it provides a bound for the fixed-beamformer array-design problem, while the obtained activation vector may contain fractional entries and cannot yet be applied to the physical switch network.

5.4 Binary Recovery and Feasibility Restoration

To obtain a physically feasible array configuration, we employ deterministic rounding together with Gaussian randomisation. The deterministic rule activates the $S_{\max}$ largest entries of the relaxed vector. For Gaussian randomisation, the covariance of the relaxed activation variable is constructed as

$$\boldsymbol{\Sigma}_a = \boldsymbol{A}^\star - \boldsymbol{a}^\star (\boldsymbol{a}^\star)^{\mathsf{T}} \succeq \boldsymbol{0} \tag{5.34}$$

as the relaxed covariance and generates L samples

$$\boldsymbol{\xi}_\ell \sim \mathcal{N}(\boldsymbol{a}^\star, \boldsymbol{\Sigma}_a), \qquad \ell = 1,\ldots,L. \tag{5.35}$$

For each sample, the $S_{\max}$ largest entries are set to one and the remaining entries are set to zero. Duplicate layouts are removed to avoid unnecessary beamforming updates.

Rounding does not preserve the relaxed QoS constraints automatically. Therefore, each binary candidate is passed back to Subproblem 1. Its beamformers are re-optimised, and candidates that violate C1 or C2 are discarded. Among the feasible candidates, the one with the largest value of the *original* objective (4.1a) is selected. This feasibility-restoration step prevents an apparently strong relaxed point from being reported as a physical solution.

5.5 Overall Suboptimal Algorithm

To summarise, the proposed low-complexity solution consists of an outer AO loop and two inner SCA procedures. The complete implementation is presented in Algorithm 1. Each reported iterate corresponds to a binary layout and recovered beamforming vectors that satisfy the original constraints; relaxed matrix objectives are used only to guide the updates.

Algorithm 1 Joint NUSA selection and beamforming via AO–SCA–SDR

Input: channels, target parameters, $P_{\max}$, $S_{\max}$, $\{\gamma_k\}$, λ, tolerances $\varepsilon_{\mathrm{SCA}}$ and $\varepsilon_{\mathrm{AO}}$, and sample count L.
Find an initial feasible binary layout $\boldsymbol{a}^{(0)}$ and beamformers $\{\boldsymbol{w}_k^{(0)}\}$; set $r = 0$.
repeat
    Fix $\boldsymbol{a} = \boldsymbol{a}^{(r)}$.
    repeat
        Construct the tangent bounds (5.11) at $\{\boldsymbol{W}_i^{(t)}\}$.
        Solve the convex SDP (5.16); set $t \leftarrow t+1$.
    until the Subproblem 1 objective change is at most $\varepsilon_{\mathrm{SCA}}$
    Recover $\{\boldsymbol{w}_k^{(r+1)}\}$ from $\{\boldsymbol{W}_k^{\star}\}$ and verify C1–C2.
    Fix $\{\boldsymbol{w}_k\} = \{\boldsymbol{w}_k^{(r+1)}\}$.
    repeat
        Construct the tangent bounds (5.29) at $\boldsymbol{A}^{(t)}$.
        Solve the convex SDP (5.33); set $t \leftarrow t+1$.
    until the Subproblem 2 relaxed objective change is at most $\varepsilon_{\mathrm{SCA}}$
    Generate deterministic and Gaussian-randomised binary layouts.
    Re-solve Subproblem 1 for each layout and retain the best feasible pair.
    Accept the pair if its original objective is no smaller than the incumbent; set $r \leftarrow r+1$.
until the relative incumbent improvement is at most $\varepsilon_{\mathrm{AO}}$
return $\boldsymbol{a}^{\star}$ and $\{\boldsymbol{w}_k^{\star}\}$.

An initial feasible point can be obtained by solving the beamforming feasibility problem for the full array and then pruning low-power elements one at a time until $S_{\max}$ remains. Several random sparse layouts can be tested if pruning fails. If none is feasible, the specified SINR thresholds, power budget, and RF-chain limit are mutually incompatible for the given channel realisation.

5.6 Convergence Analysis

The convergence of the proposed scheme follows from the tightness properties of the SCA surrogates. The tangent approximation of each subtracted logarithm is a global upper bound, coincides with the original function at the current iterate, and has the same first-order derivative. Consequently, (5.12) and (5.29) constitute locally tight lower bounds on the original user rate. The solution from the current SCA iteration remains feasible for the next surrogate problem; hence, the relaxed objective generated within each block is non-decreasing. Since C2 bounds the transmit covariance and C3 bounds the active aperture, this sequence is also bounded above and therefore converges to a stationary point of the corresponding relaxed block problem under the standard SCA regularity conditions [57].

For the outer AO loop, exact optimisation of each original block would give

$$O(\boldsymbol{a}^{(r)}, \boldsymbol{W}^{(r+1)}) \geq O(\boldsymbol{a}^{(r)}, \boldsymbol{W}^{(r)}), \tag{5.36}$$

$$O(\boldsymbol{a}^{(r+1)}, \boldsymbol{W}^{(r+1)}) \geq O(\boldsymbol{a}^{(r)}, \boldsymbol{W}^{(r+1)}), \tag{5.37}$$

and hence a monotone bounded sequence. SDR and binary recovery complicate the second inequality because rounding can reduce the objective or destroy feasibility. Algorithm 1 restores the monotonic property by accepting a recovered binary point only if it is feasible and no worse than the incumbent. Thus, the stored feasible objective sequence is non-decreasing and bounded, and must converge. This result does not establish global optimality: the limit is a stationary/suboptimal solution determined by the initial point, relaxations, and candidate recovery.

5.7 Computational Complexity Analysis

Let d_q be the dimension of $\boldsymbol{F}_q$, I_{BF} and I_{AS} the SCA iteration counts for the two blocks, and I_{AO} the outer iteration count.

Subproblem 1 contains K Hermitian $N \times N$ matrices and Q Hermitian $d_q \times d_q$ epigraph matrices. Its real scalar-variable order is

$$n_{\mathrm{BF}} = O\left(KN^2 + \sum_{q=1}^{Q} d_q^2 \right). \tag{5.38}$$

It contains K QoS inequalities, one power inequality, K PSD cones of size N, and Q Schur-

complement cones of size $2d_q$. A generic interior-point estimate is

$$C_{\mathrm{BF}} = O\left(n_{\mathrm{BF}}^{3.5} \log \frac{1}{\varepsilon_1}\right), \tag{5.39}$$

where ε_1 is the solver accuracy.

Subproblem 2 contains one $N \times N$ matrix, one N-vector, and the sensing epigraph matrices, giving

$$n_{\mathrm{AS}} = O\left(N^2 + N + \sum_{q=1}^{Q} d_q^2\right). \tag{5.40}$$

The lifted $(N+1) \times (N+1)$ cone dominates for large N, producing the familiar worst-case SDP scaling

$$C_{\mathrm{AS}} = O\left(N^{6.5} \log \frac{1}{\varepsilon_2}\right) \tag{5.41}$$

up to lower-order terms associated with QoS and sensing LMIs. Gaussian randomisation requires $O(LN^2)$ operations to sample and rank the candidates, excluding the subsequent beamforming feasibility solves.

The complete algorithm therefore has approximate complexity

$$C_{\mathrm{total}} = O(I_{\mathrm{AO}} [I_{\mathrm{BF}} C_{\mathrm{BF}} + I_{\mathrm{AS}} C_{\mathrm{AS}} + L C_{\mathrm{check}}]), \tag{5.42}$$

where C_{check} includes beamforming recovery and feasibility restoration for one binary layout. The antenna-selection SDP is expected to dominate when the candidate grid is large. Warm starts, removal of duplicate randomisations, and screening candidates with inexpensive QoS bounds are therefore important implementation measures.

5.8 Implementation and Reproducibility Requirements

Every reported result must be evaluated from the original binary activation vector and recovered beamformers. The simulation record should include the candidate geometry, active-element budget, user and target positions, channel model, noise powers, QoS thresholds, λ, solver and version, SCA/AO tolerances, randomisation count, channel-realisation count, and random seed. Relaxed SDP objectives should be labelled as bounds and must not be compared directly with feasible benchmark values without explanation.

Chapter 6

Simulation Results and Discussion

In this chapter, simulation results are presented to demonstrate the effectiveness of the proposed dynamic NUSA design and to investigate the influence of the principal system parameters on communication and sensing performance. Unless otherwise specified, the simulation parameters are set as summarised in Table 6.1. A fixed channel bank is generated with random seed 2025 and is used consistently throughout the simulations. Subproblems 1 and 2 are implemented in CVX and solved using SDPT3 and SeDuMi, respectively. All reported performance values are recomputed from the recovered binary activation vector and its refined beamformers according to the original objective function.

Table 6.1: Default simulation parameters.

Parameter	Value
Number of candidate antenna positions, N	16
Number of communication users, K	2
Target direction	15°
Channel model	Racian fading
Common large-scale channel power gain	-70 dB
Maximum number of active antennas, $S_{\max}$	10
Maximum transmit power, $P_{\max}$	30 dBm
Noise power, σ^2	10^{-10} W
Minimum user SINR, γ_k	0.1
Communication–sensing weight, λ	500
Maximum number of AO iterations	10
Maximum fixed-topology refinements	8
Relative convergence tolerance	10^{-4}
Gaussian randomisation trials	40
Retained Gaussian candidates	10
Random channel seed	2025

For comparison, a random sparse array is adopted as the baseline scheme. For a given $S_{\max}$, 20 unique layouts are generated by selecting exactly $S_{\max}$ positions uniformly at random from the same N candidate locations. The baseline is not evaluated with arbitrary or unoptimised transmit weights. Instead, for each random layout, the antenna topology is fixed and the corresponding beamformers are reoptimised using Subproblem 1 under the same transmit-power and user-QoS constraints as the proposed scheme. The baseline result is the arithmetic mean over all feasible random layouts. Therefore, both schemes employ optimised beamforming, while only the proposed NUSA jointly optimises the antenna geometry. This comparison isolates the performance gain provided by the antenna-selection block.

The convergence behaviour of the proposed algorithm is first examined. For the representative channel realisation recorded in the simulation, the relaxed objective values are 24.3161, 24.3168, and 24.3170 in three successive AO iterations. Hence, the objective increases monoton-

ically and converges within three iterations under the prescribed tolerance. After binary recovery and fixed-topology refinement, the feasible objective is 18.2307. The difference between the relaxed and feasible values results from enforcing binary antenna states and recovering an implementable topology from the semidefinite relaxation. These observations are consistent with the convergence analysis in Chapter 5 and show that the proposed algorithm can reach a stable solution with a small number of outer iterations.

Fig. 6.1 compares the communication sum rate and sensing CRB of the proposed NUSA with those of the random sparse baseline over five paired channel realisations. As shown in Fig. 6.1(a), the proposed scheme achieves a higher communication sum rate in every realisation. The average sum rates of the random sparse baseline and proposed NUSA are 10.2289 and 17.3172 bit/s/Hz, respectively, corresponding to a 69.30% improvement. In particular, the rate gains in the five realisations range from 46.51% to 85.25%. This is because the proposed scheme jointly adjusts the antenna topology and transmit beamformers according to the instantaneous communication channels, whereas the baseline can only optimise the beamformers over a randomly prescribed aperture.

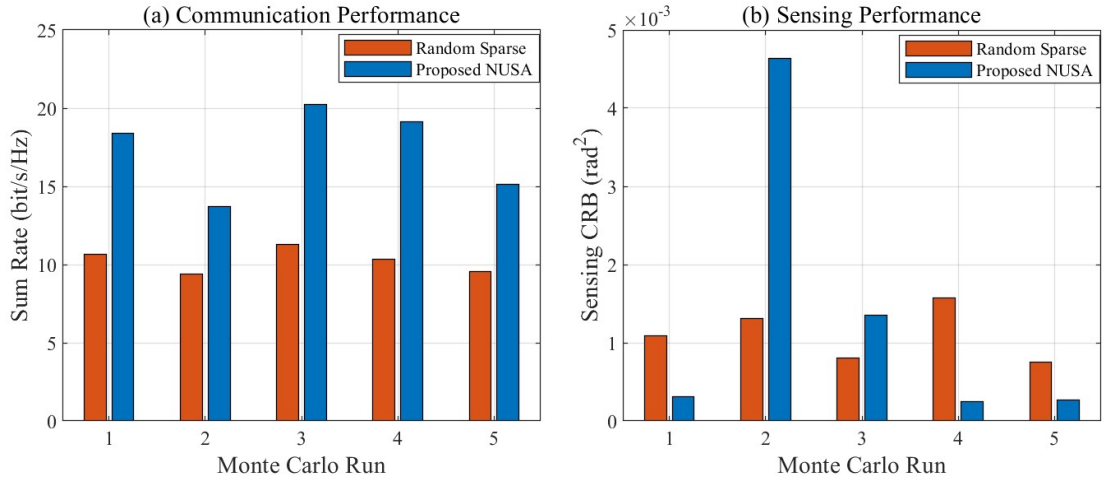

Figure 6.1: Communication sum rate and sensing CRB of the proposed NUSA and the random sparse baseline.

Fig. 6.1(b) further illustrates the sensing performance. The proposed scheme obtains a lower CRB in the first, fourth, and fifth realisations. In these cases, optimising the element positions forms a more informative aperture along the target direction and increases the angular Fisher information. In the second and third realisations, the proposed solution allocates more of the available design freedom to communication enhancement and consequently yields a larger CRB

than the random-layout mean. The median CRB nevertheless decreases from 1.0894×10^{-3} for the baseline to 3.1229×10^{-4} for the proposed scheme. When both metrics are incorporated into the objective $U_{\text{comm}} - \lambda J_{\text{sense}}$, the proposed and baseline schemes achieve average objective values of 16.6352 and 9.6758, respectively. Thus, the proposed joint design improves the average objective by 71.93%, demonstrating its overall advantage in balancing communication and sensing performance.

Fig. 6.2 presents the optimised per-antenna transmit-power distributions. The recovered numbers of active elements in the five channel realisations are 10, 8, 6, 9, and 10, which confirms that the proposed method does not necessarily exhaust the available RF-chain budget. Moreover, the selected supports vary with the channel realisation. For example, antenna position 10 remains inactive, whereas positions 1, 8, and 16 are repeatedly selected. This illustrates that a single fixed sparse layout is not equally suitable for different propagation environments.

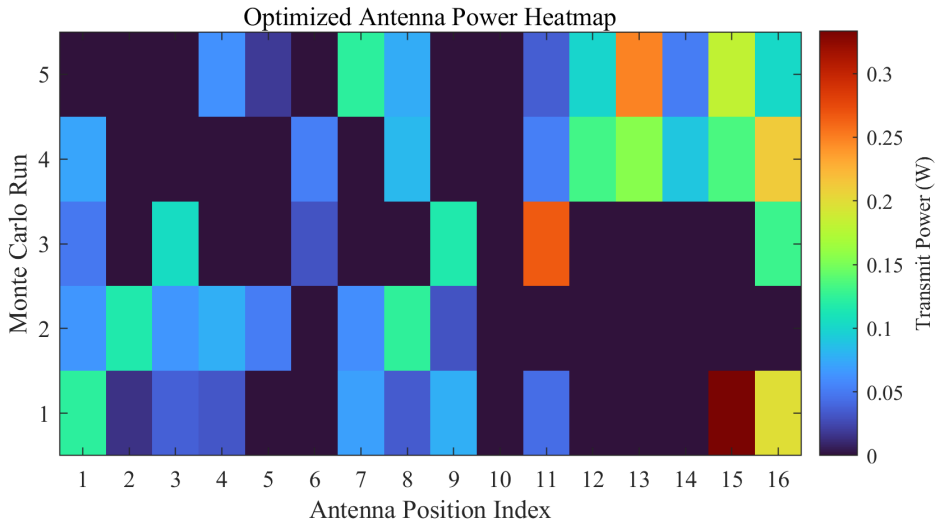

Figure 6.2: Optimised per-antenna transmit-power distributions over five channel realisations.

It can also be observed that the power is distributed non-uniformly over the selected positions. In the first realisation, approximately 0.333 W and 0.198 W are assigned to positions 15 and 16, respectively, while several other active elements carry less than 0.05 W. In fact, antenna activation determines the available spatial aperture, while the beamformers determine how the transmit power is distributed within that aperture. The channel-dependent support and power patterns in Fig. 6.2 therefore verify the necessity of jointly optimising antenna selection and beamforming.

In Fig. 6.3, the effect of the maximum number of active antennas is investigated. As shown

in Fig. 6.3(a), the communication sum rate of the proposed scheme increases from 13.0267 to 26.0528 bit/s/Hz as $S_{\max}$ increases from 5 to 15. The proposed scheme outperforms the random sparse baseline for every tested antenna budget. When $S_{\max}$ is small, the performance gap is particularly pronounced because each selected position has a strong influence on the effective aperture and multi-user interference suppression. As $S_{\max}$ approaches the total number of candidate positions, the baseline has less opportunity to select a severely unfavourable topology, and the communication-performance gap consequently becomes smaller.

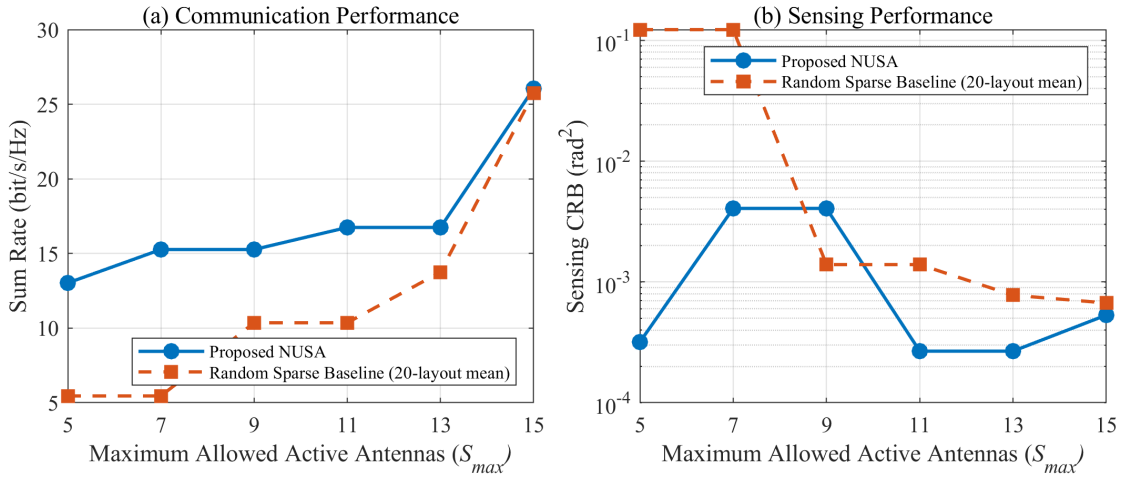

Figure 6.3: Communication and sensing performance versus the maximum number of active antennas.

Fig. 6.3(b) shows that the sensing performance is highly sensitive to the selected geometry. At $S_{\max} = 5$, the proposed scheme achieves a CRB of approximately 3×10^{-4} rad^2, while the random sparse baseline yields approximately 1.227×10^{-1} rad^2. Hence, optimising a small number of antenna positions can preserve substantial angular information that is easily lost under random selection. The CRB of the proposed scheme is not strictly monotonic because the optimisation maximises the joint weighted objective rather than minimising the sensing term independently. For $S_{\max} = 7$ and 9, a communication-favourable recovered topology increases the rate while producing a higher CRB. When $S_{\max}$ increases to 11 and 13, the additional spatial flexibility enables the algorithm to reduce the CRB to approximately 3×10^{-4} rad^2 while maintaining a higher communication rate. These results demonstrate that the exact sparse geometry, rather than the number of active elements alone, determines the communication–sensing balance.

Fig. 6.4 depicts the joint objective versus the maximum transmit power. It is evident that

the objective values of both schemes increase as $P_{\max}$ increases. This is because a larger power budget strengthens the desired communication signals and target illumination, thereby improving the achievable sum rate and reducing the weighted sensing penalty. The proposed objective increases from 12.1908 at 20 dBm to 33.8790 at 44 dBm, whereas the random sparse mean increases from -43.4686 to 17.9306. The negative baseline objective in the low-power regime occurs because the weighted CRB penalty is larger than the available communication utility.

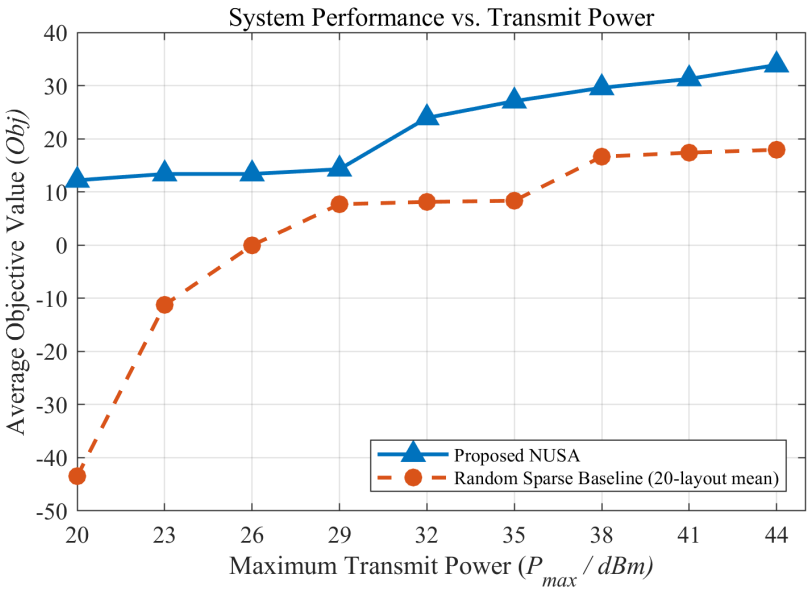

Figure 6.4: Joint objective versus the maximum transmit power.

Furthermore, the proposed scheme achieves the highest objective across all tested power budgets. In the low-power regime, optimising the antenna geometry allows the limited transmit power to be directed through spatially informative positions, avoiding the severe sensing penalty experienced by typical random layouts. At higher power, both schemes benefit from the increased signal strength, but the proposed scheme retains a substantial advantage because the additional power is allocated jointly with the array geometry and beamformers. This verifies that dynamic sparse-array design can utilise the available transmit power more effectively than random antenna activation.

Fig. 6.5 illustrates the relationship between communication sum rate and sensing CRB when the weighting coefficient is varied over $\lambda \in \{1, 10, 100, 500, 1000, 2000, 5000, 10000\}$. A small value of λ places relatively little emphasis on sensing accuracy and can therefore produce a large CRB. For example, the CRB is approximately 7.9×10^{-3} at $\lambda = 1$. By contrast, the smallest observed CRB is approximately 2×10^{-4} at $\lambda = 10^4$, demonstrating that increasing the sensing

weight can direct the optimisation towards a more sensing-informative solution.

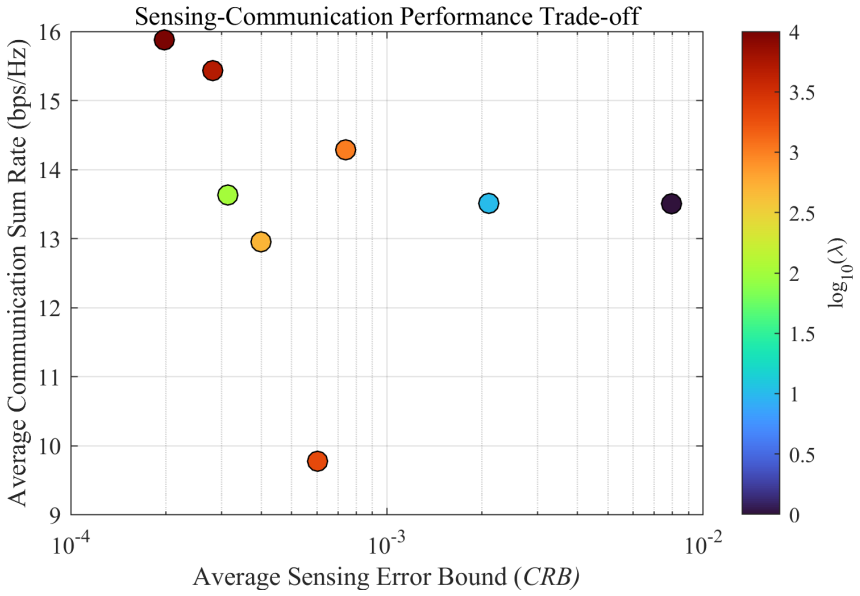

Figure 6.5: Communication sum rate versus sensing CRB for different values of λ.

The obtained points do not form a strictly monotonic curve. In particular, the solution at $\lambda = 5000$ achieves a higher rate and a lower CRB than that obtained at $\lambda = 2000$. This behaviour arises because the original problem is mixed-integer and non-convex: different weighting coefficients may lead the AO iterations and binary recovery to different stationary points and antenna cardinalities. Nevertheless, the overall movement from the sensing-poor solution at small λ towards lower-CRB operating points at large λ confirms that the weighting coefficient provides an effective mechanism for controlling the communication–sensing preference. Multiple initialisations or a continuation strategy can be employed when a smoother approximation of the trade-off boundary is required.

Overall, the simulation results validate the effectiveness of the proposed dynamic NUSA framework. Compared with random sparse activation followed by optimised beamforming, the proposed joint design substantially improves the communication sum rate and weighted objective, particularly when antenna and power resources are limited. The selected antenna supports and power distributions adapt to the propagation environment, and the results for $S_{\max}$ show that the arrangement of the active elements is as important as their number. Moreover, varying $P_{\max}$ and λ demonstrates that the proposed algorithm can effectively exploit additional transmit resources and adjust the balance between communication quality and sensing accuracy. These observations confirm the value of treating antenna geometry and beamforming as coupled

optimisation variables in sparse MIMO-ISAC systems.

Chapter 7

Conclusion and Future Work

This thesis investigated the joint design of dynamic non-uniform sparse antenna arrays and transmit beamforming for multi-user MIMO-ISAC systems. To improve communication performance and sensing accuracy under limited hardware resources, the antenna activation pattern was treated as an optimisable system variable rather than a prescribed array structure. A weighted optimisation problem was formulated to maximise the communication sum rate while reducing the sensing CRB, subject to the minimum user SINR, total transmit-power, active-RF-chain, and binary antenna-selection constraints. The resulting problem is mixed-integer and non-convex because the antenna states and beamformers are coupled in the communication powers, transmit covariance, and sensing information.

To address this problem, an AO-based suboptimal algorithm was developed. With the antenna activation pattern fixed, the beamforming subproblem was transformed using matrix lifting, SCA, and SDR. With the beamformers fixed, the antenna-selection subproblem was handled through an augmented matrix representation, SCA, and semidefinite relaxation. Top-s selection, threshold recovery, and Gaussian randomisation were then employed to recover feasible binary antenna layouts, followed by fixed-topology beamforming refinement. The convergence and computational complexity of the complete algorithm were also analysed. In particular, the locally tight SCA approximations and feasible-incumbent acceptance rule generate a stable non-decreasing objective sequence, although global optimality cannot be guaranteed for the original mixed-integer problem.

The numerical results validated the effectiveness of the proposed framework. Compared with a random sparse baseline in which the beamformers were separately optimised for each topology, the proposed NUSA increased the average communication sum rate from 10.2289 to

17.3172 bit/s/Hz and improved the average weighted objective by 71.93%. The proposed design achieved a higher communication rate in all five paired channel realisations and obtained a lower sensing CRB in three of them. The antenna-budget results further showed that optimising a small number of positions can preserve angular information that is lost under random activation, while the power-budget results confirmed that the proposed scheme can utilise additional transmit power more effectively. Furthermore, the recovered antenna supports and power distributions changed with the channel realisation, demonstrating the adaptive nature of the proposed design.

These findings confirm that sparse-array geometry and transmit beamforming should be designed jointly in an ISAC system. Merely increasing the number of active elements does not necessarily provide the best sensing performance, since the Fisher information depends strongly on the spatial distribution of those elements. By adapting the active aperture to the current communication channels and sensing direction, the proposed framework provides a flexible means of balancing spectral efficiency, sensing accuracy, and RF-chain usage.

Several extensions merit further investigation. First, robust optimisation can be incorporated to account for imperfect channel state information, target-angle uncertainty, mutual coupling, and switching losses. Second, the design can be extended to multiple sensing targets and more general planar candidate arrays, where azimuth, elevation, delay, Doppler, and reflection coefficients are estimated jointly. Third, continuation, multi-start recovery, or learning-assisted initialisation may reduce sensitivity to local stationary points and improve the rate–CRB boundary. Recent deep-reinforcement-learning-based beamforming for reconfigurable antenna systems [59] further motivates training low-complexity learning models, such as graph neural networks, using solutions generated by the proposed optimisation algorithm, thereby enabling rapid antenna selection in time-varying environments. Experimental validation with measured channels and practical RF switching hardware will also be important for assessing the proposed framework under realistic deployment conditions.

Bibliography

[1] K. Meng, C. Masouros, A. P. Petropulu, and L. Hanzo, "Cooperative ISAC networks: Opportunities and challenges," *IEEE Wireless Communications*, vol. 32, no. 3, pp. 212–219, 2025. [Online]. Available: https://ieeexplore.ieee.org/document/10726912/

[2] F. Liu, C. Masouros, A. P. Petropulu, H. Griffiths, and L. Hanzo, "Joint radar and communication design: Applications, state-of-the-art, and the road ahead," *IEEE Transactions on Communications*, vol. 68, no. 6, pp. 3834–3862, 2020. [Online]. Available: https://ieeexplore.ieee.org/document/8999605

[3] M. Banafaa, I. Shayea, J. Din, M. Hadri Azmi, A. Alashbi, Y. Ibrahim Daradkeh, and A. Alhammadi, "6G mobile communication technology: Requirements, targets, applications, challenges, advantages, and opportunities," *Alexandria Engineering Journal*, vol. 64, pp. 245–274, 2023. [Online]. Available: https://www.sciencedirect.com/science/article/pii/S111001682200549X

[4] Z. He, W. Xu, H. Shen, D. W. K. Ng, Y. C. Eldar, and X. You, "Full-duplex communication for ISAC: Joint beamforming and power optimization," *IEEE Journal on Selected Areas in Communications*, vol. 41, no. 9, pp. 2920–2936, 2023. [Online]. Available: https://ieeexplore.ieee.org/document/10158711/

[5] A. M. Elbir, K. V. Mishra, and A. C. GürbüZ, "Deep sparse array design for integrated sensing and communications," in *2023 IEEE International Radar Conference (RADAR)*, 2023, pp. 1–5. [Online]. Available: https://ieeexplore.ieee.org/document/10371037

[6] K. Takeuchi. (2016) Asymptotic optimality of massive MIMO systems using densely spaced transmit antennas. [Online]. Available: http://arxiv.org/abs/1601.05873

[7] X. Li, H. Min, Y. Zeng, S. Jin, L. Dai, Y. Yuan, and R. Zhang, "Sparse MIMO for ISAC: New opportunities and challenges," *IEEE Wireless Communications*, vol. 32, no. 4, pp. 170–178, 2025. [Online]. Available: https://ieeexplore.ieee.org/document/10930389

[8] H. Wang, C. Feng, Y. Zeng, S. Jin, C. Yuen, B. Clerckx, and R. Zhang, "Enhancing spatial multiplexing and interference suppression for near- and far-field communications with sparse MIMO," 2024. [Online]. Available: http://arxiv.org/abs/2408.01956

[9] R. P. Sankar and S. P. Chepuri, "Sparse array and precoding design for integrated sensing and communication systems," in *2024 IEEE 13rd Sensor Array and Multichannel Signal Processing Workshop (SAM)*, 2024, pp. 1–5. [Online]. Available: https://ieeexplore.ieee.org/abstract/document/10636359

[10] Z. Gao, Z. Wan, D. Zheng, S. Tan, C. Masouros, D. W. K. Ng, and S. Chen, "Integrated sensing and communication with mmWave massive MIMO: A compressed sampling perspective," *IEEE Transactions on Wireless Communications*, vol. 22, no. 3, pp. 1745–1762, 2023. [Online]. Available: https://ieeexplore.ieee.org/document/9898900

[11] Y. Liu, C. Pan, X. Liu, Y. Zhu, and Y. Liu, "A waveform design for MIMO sensing on two-dimensional arrays with sparse estimation," *Electronics*, vol. 12, no. 18, p. 3906, 2023. [Online]. Available: https://www.mdpi.com/2079-9292/12/18/3906

[12] S. G. Tanyer, P. Dent, M. Ali, C. Davis, S. Rajagopal, and P. F. Driessen, "Multi-objective design and optimization of hardware-friendly grid-based sparse MIMO arrays," *Sensors*, vol. 24, no. 21, p. 6810, 2024. [Online]. Available: https://www.mdpi.com/1424-8220/24/21/6810

[13] Z. Wang, J. Zhang, W. Yi, H. Xiao, H. Du, D. Niyato, B. Ai, and D. W. K. Ng, "Analytical Framework for Effective Degrees of Freedom in Near-Field XL-MIMO," *IEEE Trans. Wireless Commun.*, vol. 24, pp. 3465–3482, 2025.

[14] M. Sun, Y. Gong, R. Zhang, Y. Zhao, X. Jing, C. Yuen, and D. W. K. Ng, "Robust Spherical Wavefront Beamforming for Near-Field ISAC with MMSE Optimization: A Distance-Angle Perspective," *IEEE Trans. Commun.*, vol. 74, pp. 6718–6733, 2026.

[15] X. Shao, L. Hu, Y. Sun, X. Li, Y. Zhang, J. Ding, X. Shi, F. Chen, D. W. K. Ng, and R. Schober, "Hybrid Near-Far Field 6D Movable Antenna Design Exploiting Directional

Sparsity and Deep Learning," *IEEE Trans. Wireless Commun.*, vol. 25, pp. 3736–3749, 2026.

[16] S. Hou, Y. Wang, T. Zeng, and S. Wu, "Sparse channel estimation for spatial non-stationary massive MIMO channels," *IEEE Communications Letters*, vol. 24, no. 3, pp. 681–684, Mar. 2020.

[17] Z. Ren, L. Qiu, J. Xu, and D. W. K. Ng, "Sensing-Assisted Sparse Channel Recovery for Massive Antenna Systems," *IEEE Trans. Veh. Technol.*, vol. 73, no. 11, pp. 17 824–17 829, 2024.

[18] S. Liu, X. Yu, Z. Gao, J. Xu, D. W. K. Ng, and S. Cui, "Sensing-Enhanced Channel Estimation for Near-Field XL-MIMO Systems," *IEEE J. Sel. Areas Commun.*, vol. 43, pp. 628–643, 2025.

[19] H. Lei, J. Zhang, Z. Liu, H. Xiao, B. Ai, D. W. K. Ng, and A. Nallanathan, "Low-Complexity Channel Estimation for Spatial Non-Stationary XL-MIMO Systems: A Model-Based Deep Learning Approach," *IEEE Trans. Commun.*, 2026.

[20] J. Lu, J. Zhang, H. Lei, H. Xiao, B. Ai, and D. W. K. Ng, "Near-field Spatial-domain Channel Extrapolation for XL-MIMO Systems," *IEEE Trans. Wireless Commun.*, vol. 25, pp. 4343–4357, 2026.

[21] Y. Chu, Z. Wei, Z. Yang, and D. W. K. Ng, "Channel Estimation for RIS-Aided MIMO Systems: A Partially Decoupled Atomic Norm Minimization Approach," *IEEE Trans. Wireless Commun.*, vol. 23, no. 11, pp. 16 048–16 061, 2024.

[22] Q. Xu, L. Lan, T.-X. Zheng, F. Liu, G. Liao, and D. W. K. Ng, "Transceiver Optimization of FDA-MIMO Radar-Communication Coexistence Systems," *IEEE Trans. Commun.*, 2026.

[23] A. Khalili, M. R. Mili, S. Parsaeefard, M. Rasti, and D. W. K. Ng, "Antenna Selection Strategy for Energy Efficiency Maximization in Uplink OFDMA Networks: A Multi-objective Approach," *IEEE Trans. Wireless Commun.*, vol. 19, no. 1, pp. 595–609, 2020.

[24] W. Yuan, Z. Wei, S. Li, J. Yuan, and D. W. K. Ng, "Integrated Radar Sensing and Communication-assisted Orthogonal Time Frequency Space Transmission for Vehicular Networks," *IEEE J. Sel. Topics Signal Process.*, vol. 15, no. 6, pp. 1515–1528, 2021.

[25] S. Li, W. Yuan, C. Liu, Z. Wei, J. Yuan, B. Bai, and D. W. K. Ng, "A Novel ISAC Transmission Framework based on Spatially-Spread Orthogonal Time Frequency Space Modulation," *IEEE J. Sel. Areas Commun.*, vol. 40, no. 6, pp. 1854–1872, 2022.

[26] J. Wu, W. Yuan, Z. Wei, K. Zhang, F. Liu, and D. W. K. Ng, "Low-Complexity Minimum BER Precoder Design for ISAC Systems: A Delay-Doppler Perspective," *IEEE Trans. Wireless Commun.*, vol. 24, pp. 1526–1540, 2025.

[27] Z. Xiao, Y. Zeng, F. Wen, Z. Zhang, and D. W. K. Ng, "Integrated Sensing and Channel Estimation by Exploiting Dual Timescales for Delay-Doppler Alignment Modulation," *IEEE Trans. Wireless Commun.*, vol. 24, pp. 415–429, 2025.

[28] W. Yuan, F. Liu, C. Masouros, J. Yuan, D. W. K. Ng, and N. González-Prelcic, "Bayesian Predictive Beamforming for Vehicular Networks: A Low-overhead Joint Radar-Communication Approach," *IEEE Trans. Wireless Commun.*, vol. 20, no. 3, pp. 1442–1456, 2021.

[29] C. Liu, W. Yuan, S. Li, X. Liu, H. Li, D. W. K. Ng, and Y. Li, "Learning-based Predictive Beamforming for Integrated Sensing and Communication in Vehicular Networks," *IEEE J. Sel. Areas Commun.*, vol. 40, no. 8, pp. 2317–2334, 2022.

[30] M. Huang, M. Yin, and H. Xu, "Analysis on UAV sensing with sparse array in ISAC system," in *2025 IEEE Wireless Communications and Networking Conference (WCNC)*, 2025, pp. 1–6. [Online]. Available: https://ieeexplore.ieee.org/document/10978166/

[31] H. Lei, J. Zhang, H. Xiao, D. W. K. Ng, and B. Ai, "Deep Learning Based Near-Field User Localization with Beam Squint in Wideband XL-MIMO Systems," *IEEE Trans. Wireless Commun.*, vol. 24, pp. 1568–1583, 2025.

[32] S. Yu, W. Shi, W. Xu, D. W. K. Ng, and N. Al-Dhahir, "Disentangling Dual-Polarized Channel Representations for Accurate User Localization," *IEEE Trans. Commun.*, 2026.

[33] M. Xia, Z. He, W. Xu, Y. Huang, D. W. K. Ng, and N. Al-Dhahir, "Coordinated Beamforming for Networked Integrated Communication and Multi-TMT Localization," *IEEE Trans. Commun.*, 2026.

[34] L. Wang, Y. Cai, X. Li, and S. Hu, "Joint beamforming and port selection for fluid antenna-assisted nearshore ISAC systems," in *Proc. 20th Int. Symp. Wireless Commun. Syst. (ISWCS)*, Aug. 2026, accepted for publication.

[35] R. Zhao, Y. Zhang, S. Hu, and D. W. K. Ng, "Pinching antenna-assisted ISAC with waveguide mode selection," in *Proc. 20th Int. Symp. Wireless Commun. Syst. (ISWCS)*, Aug. 2026, accepted for publication.

[36] D. Bepari, S. Mondal, A. Bhowal, K. Singh, H. Shin, K.-K. Wong, and D. W. K. Ng, "Fluid Antennas: Pioneering a New Era in Next-Generation Wireless Communications," *IEEE Commun. Surveys Tuts.*, vol. 28, pp. 5596–5631, 2026.

[37] X. Chen, B. Feng, Y. Wu, D. W. K. Ng, and R. Schober, "Two-Timescale Sum-Rate Maximization for Movable Antenna Enhanced Systems," *IEEE Trans. Wireless Commun.*, vol. 25, pp. 3894–3909, 2026.

[38] B. Xu, J. Zhang, S. Chen, Z. Liu, H. Xiao, D. W. K. Ng, and B. Ai, "Multi-Agent Reinforcement Learning for Movable Antenna-aided Cell-Free Massive MIMO Systems," *IEEE J. Sel. Areas Commun.*, 2026.

[39] X. Zhang, L. Xiang, J. Wang, X. Gao, D. W. K. Ng, and R. Schober, "Rotatable Antenna Array Enabled UAV mmWave Massive MIMO Communication," *IEEE Trans. Commun.*, vol. 74, pp. 1219–1236, 2026.

[40] D. Wang, E. Shi, J. Zhang, J. An, D. W. K. Ng, and B. Ai, "Joint Precoding and Surface Morphing Design for Flexible Intelligent Metasurfaces-Aided Cell-Free Massive MIMO Systems," *IEEE Trans. Veh. Technol.*, pp. 1–6, 2026.

[41] W. Wang, D. Qiao, L. Yang, Y. Zhan, and D. W. K. Ng, "Optimal Resource Allocation Design for Wideband Integrated Sensing and Communication Systems," *IEEE Trans. Wireless Commun.*, vol. 24, pp. 2140–2156, 2025.

[42] W. Hu, Z. He, W. Xu, Y. Huang, D. W. K. Ng, and N. Al-Dhahir, "Energy-Efficient Hybrid Beamfocusing for Near-Field Integrated Sensing and Communication," *IEEE Trans. Signal Process.*, vol. 73, pp. 4011–4026, 2025.

[43] X. Song, X. Yu, J. Xu, and D. W. K. Ng, "CRB-Rate Tradeoff for Bistatic ISAC with Gaussian Information and Deterministic Sensing Signals," *IEEE Trans. Wireless Commun.*, vol. 25, pp. 11 768–11 782, 2026.

[44] W. Mao, Y. Lu, G. Pan, J. An, B. Ai, and D. W. K. Ng, "Cramér-Rao Bound Optimization for Bistatic ISAC: Transceiver Design and Attention-Based ISACNet," *IEEE J. Sel. Areas Commun.*, vol. 44, pp. 181–195, 2026.

[45] J. Zhang, S. Gong, W. Lu, C. Xing, N. Zhao, D. W. K. Ng, and D. Niyato, "Joint Design for STAR-RIS Aided ISAC: Decoupling or Learning," *IEEE Trans. Wireless Commun.*, vol. 23, no. 10, pp. 14 365–14 379, 2024.

[46] X. Zhou, F. Ke, C. Wu, X. Y. Zhang, and D. W. K. Ng, "Robust Beamforming for STAR-RIS aided Hybrid-Field ISAC Systems," *IEEE Trans. Commun.*, vol. 74, pp. 5654–5669, 2026.

[47] X. Zhou, F. Ke, X. Y. Zhang, F. Gao, Y. Zhai, B. Tang, and D. W. K. Ng, "STAR-RIS-Aided Wideband Cell-Free ISAC: Joint Resource Allocation and Beamforming," *IEEE Trans. Commun.*, 2026.

[48] X. Song, Y. Fang, F. Wang, Z. Ren, X. Yu, Y. Zhang, F. Liu, J. Xu, D. W. K. Ng, R. Zhang, and S. Cui, "An Overview on IRS-Enabled Sensing and Communications for 6G: Architectures, Fundamental Limits, and Joint Beamforming Designs," *Sci. China Inf. Sci.*, vol. 68, 2025.

[49] H. Ke, J. Xu, W. Xu, C. Ding, and D. W. K. Ng, "Rate Splitting and Beamforming Design for RIS-Assisted RSMA-Enhanced ISAC Networks," *IEEE Wireless Commun. Lett.*, vol. 14, pp. 1738–1742, 2025.

[50] T.-X. Zheng, X. Chen, L. Lan, Y. Ju, X. Hu, R. Liu, D. W. K. Ng, and T. Cui, "Reconfigurable intelligent surface-aided secure integrated radar and communication systems," *IEEE Trans. Wireless Commun.*, vol. 24, pp. 1934–1948, 2025.

[51] X. Li, Z. Wu, Y. Cai, S. Hu, Y. Liao, and W. Yuan, "Win-win of communication and sensing security for MC-NOMA ISAC systems," *IEEE Journal on Selected Areas in Communications*, vol. 43, no. 9, pp. 3214–3230, 2025.

[52] Q. Zhang, S. Yan, X. Zhou, F. Shu, D. W. K. Ng, and R. Schober, "Sensing-then-Transmit: A Two-Phase Secure ISAC Framework," *IEEE Trans. Wireless Commun.*, 2026, accepted for publication.

[53] Y. Guo, Y. Chen, Z. Ren, D. W. K. Ng, and J. Xu, "Near-Field Multi-Cell ISCAP with Extremely Large-Scale Antenna Array," *IEEE Trans. Wireless Commun.*, vol. 25, pp. 10 730–10 745, 2026.

[54] W. Mao, Y. Lu, D. Yang, B. Ai, T. Q. S. Quek, and D. W. K. Ng, "Integrated Sensing, Communication, and Power Transfer for Fluid-Antenna LEO Satellite Systems," *IEEE J. Sel. Areas Commun.*, 2026.

[55] S. M. Kay, *Fundamentals of Statistical Signal Processing: Estimation Theory*. Prentice-Hall, Inc., 1993.

[56] Z.-q. Luo, W.-k. Ma, A. M.-c. So, Y. Ye, and S. Zhang, "Semidefinite relaxation of quadratic optimization problems," *IEEE Signal Processing Magazine*, vol. 27, no. 3, pp. 20–34, 2010.

[57] B. R. Marks and G. P. Wright, "A general inner approximation algorithm for nonconvex mathematical programs," *Operations research*, vol. 26, no. 4, pp. 681–683, 1978.

[58] M. Grant and S. Boyd, "Cvx: Matlab software for disciplined convex programming, version 2.1," 2014.

[59] M. Du, S. Hu, C. Liu, and D. W. K. Ng, "Beamforming for RIS-assisted pinching antenna systems: A deep reinforcement learning approach," in *Proc. IEEE 27th Int. Workshop Signal Process. Artif. Intell. Wireless Commun. (SPAWC)*, Sep. 2026, accepted for publication.